A COMBINED COMPUTATIONAL AND EXPERIMENTAL STUDY

OF HETEROGENEOUS FRACTURE

A Thesis
Presented to
The Academic Faculty

by

Neng Wang

In Partial Fulfillment
of the Requirements for the Degree
Master of Science in Mechanical Engineering

Georgia Institute of Technology
August 2014

A COMBINED COMPUTATIONAL AND EXPERIMENTAL STUDY

OF HETEROGENEOUS FRACTURE

Approved by:

Dr. Shuman Xia, Advisor
School of Mechanical Engineering
Georgia Institute of Technology

Dr. Min Zhou
School of Mechanical Engineering
Georgia Institute of Technology

Dr. Ting Zhu
School of Mechanical Engineering
Georgia Institute of Technology

Date Approved: April 24, 2014

ACKNOWLEDGEMENTS

First, I would like to thank my advisor Dr. Shuman Xia for offering me the opportunity to study and conduct research at Georgia Tech. During the past two years, Dr. Xia not only gave me detailed guidance to the research project, but also paid a great deal of patience in teaching me the fundamentals of research. He taught me hand by hand in experimental setup, data analysis, and writing. Working with him, I have learned a lot, both professionally and personally. I really appreciate his guidance and support.

I also would like to thank my committee members: Dr. Min Zhou and Dr. Ting Zhu. Their kindness and generosity helped me to finish my degree successfully. Their knowledge and insight helped improve the quality of this thesis. I took the Elasticity course from Dr. Ting Zhu. The knowledge of this course benefited me a lot during my research.

In addition, I am grateful for the support from my lab mates: Xueju Wang, Zhipeng Pan, and Noah Dennis. It has been a great time working with them. The helpful discussion and interaction with them are vital to the progress and successful completion of this work. I will miss their company.

Last, but not least, I would like to express my deepest gratitude to my parents for their unconditional love and support. They have sacrificed so much for me since I was born. Far away from home, the conversation with them is a great encouragement for me to continue chasing my dream. In addition, their advice and experience helped me a lot when facing tough decisions. Without them, none of my success would be possible.

TABLE OF CONTENTS

LIST OF TABLES

LIST OF FIGURES

SUMMARY

Material property heterogeneity is present ubiquitously in various natural and man-made materials, such as bones, seashells, rocks, concrete, composites, and functionally graded materials. A fundamental understanding of the structure-property relationships in these material systems is crucial for the development of advanced materials with extreme properties. Well-developed homogenization schemes exist to establish such relationships in elasticity, electrostatics, magnetism, and other time- or history-independent material properties. Nevertheless, one's understanding of the effective fracture properties of heterogeneous media is remarkably limited. The challenge here is that heterogeneous fracture, as a history-dependent process, involves complex interaction and negotiation of a discontinuity front with local heterogeneities. The determination of effective fracture properties necessitates a critical interrogation of this evolutionary process in detail.

In this work, a combined experimental and modeling effort is made to examine and control fracture mechanisms in heterogeneous elastic solids. A two-phase laminated composite, which mimics the key microstructural features of many tough biological materials, is selected as a model material. In the computational part of this work, finite element analysis with cohesive zone modeling is used to model crack propagation and arrest in the laminated direction. A crack-tip-opening controlled algorithm is implemented to overcome the instability problems associated with inherently unstable crack growth. Computational results indicate that the mismatch of elastic modulus is an important factor in determining the fracture behaviors of the heterogeneous model material. Significant enhancement in the material's effective fracture toughness can be achieved with appropriate modulus mismatch. Systematic parametric studies are also performed to

investigate the effects of various material and geometrical parameters, including modulus mismatch ratio, phase volume fractions, T-stress, and cohesive zone size. Concurrently, a novel stereolithography-based additive manufacturing system is developed and used for fabricating heterogeneous test specimens with well-controlled structural and material properties. Fracture testing of each specimen is performed using the tapered double-cantilever beam (TDCB) test method. With optimized material and geometrical parameters, heterogeneous TDCB specimens are found to exhibit higher fracture toughness than their homogenous counterparts, which is in good agreement with the computational predictions.

The integrative computational and experimental study presented here provides a fundamental mechanistic understanding of the fracture mechanisms in brittle heterogeneous materials and sheds light on the rational design of ultra-tough materials through patterned heterogeneities.

CHAPTER 1

INTRODUCTION

1.1   Motivation

Many natural and man-made heterogeneous materials exhibit outstanding mechanical prosperities, such as the unusual combination of high strength and high fracture toughness. For example, natural composites, such as nacre (Yao et al. 2013), have stratified structures with microstructural heterogeneities on the nano- to micro- length scale. These composites have demonstrated exceptional mechanical properties far exceeding their individual components. Knowledge of the linkage between heterogeneous microstructure and effective mechanical properties in these material systems is crucial if we are to design and build heterogeneous materials with desired functionalities and mechanical properties. Well-developed homogenization techniques exist to establish such relationships in the context of elasticity, electrostatics, magnetism, and other time or history-independent processes.

However, one's understanding of the effective fracture properties of heterogeneous media is remarkably limited. This is because heterogeneous fracture, as a history-dependent phenomenon, involves complex interaction between a discontinuity front and local heterogeneities. The characterization of effective fracture properties necessitates a critical interrogation of this evolutionary process in detail.

This thesis is dedicated to investigate heterogeneous fracture by pursuing an integrated computational and experimental effort. Computationally, finite element analysis with cohesive zone modeling is used to model crack propagation and arrest in a two-phase

laminated composite that mimics the basic microstructural features of many tough biological materials. The experimental effort focuses on fabricating and testing heterogeneous materials with well-controlled geometrical and material parameters. The integrative computational and experimental study offers insightful guidance for designing ultra-tough materials through patterned heterogeneities.

1.2   Outline of Thesis

In Chapter 2, existing research on heterogeneous fracture and the significance of the present work are discussed. The existing research efforts focus on the study of fracture in natural and artificial heterogeneous materials. The role of modulus mismatch in fracture is highlighted. In addition, an overview of additive manufacturing technologies and their applications in fabrication of heterogeneous materials are sketched. Afterwards, the significance of the current research is pointed out.

Chapter 3 includes the computational study of fracture in heterogeneous elastic solids. In this chapter, finite element analysis with cohesive zone modeling is used to model crack propagation through a planar elastic medium with periodically varying Young's modulus. A crack-tip-opening controlled algorithm is implemented to overcome the instability problems. Comprehensive parametric studies are also carried out to explore the influence of various material and geometrical parameters, including modulus mismatch ratio, phase volume fractions, T-stress, and cohesive zone size.

The experimental efforts are presented in Chapter 4. Based on stereolithography, a novel additive manufacturing system is developed and used to fabricate both homogeneous

and heterogeneous test specimens. Homogeneous specimens are tested to characterize the mechanical properties of the individual phases in the heterogeneous materials, including elastic moduli, fracture toughness, and cohesive zone parameters. Fracture tests are performed on heterogeneous specimens to investigate their fracture behaviors. The experimental results are compared with computational modeling at the end of the chapter.

Finally, the outcomes of the present research are summarized in Chapter 5. These concluding remarks are complemented with the directions for future work.

CHAPTER 2

BACKGROUND

2.1 Fracture of Heterogeneous Solids

In the quest for advanced materials with exceptional mechanical properties, heterogeneous materials are good candidates and have attracted enormous research interest. Some of the existing efforts to address this issue are motivated by the development of high-performance ceramics or ceramic matrix composites (CMCs), whose mechanical properties are directly related to their microstructural heterogeneities. Ceramics have been widely used as structural and functional materials for their superior hardness, wear-resistance, and chemical and thermal reliability. The practical use of ceramics, however, is often limited by their inherent brittleness and low fracture toughness. Different methods have been employed to produce ceramics with high toughness. The toughening mechanisms for ceramics (Wiederhorn 1984, Hutchinson 1989, Clegg et al. 1990, Steinbrech 1992, Ighodaro and Okoli 2008, Reddy et al. 2012) vary from the traditional approaches of transformation toughening, secondary phase toughening, micro-crack toughening, and weak interfaces toughening to the more recent method of nanoporosity toughening.

Transformation toughening is also known as crack-tip shielding (Hannink and Swain 1994). This mechanism was first discussed in the work of Claussen (1976), where he discovered that Al_2O_3 composite containing 15% ZrO_2 (volume fraction) exhibited a high fracture toughness twice that of the Al_2O_3 matrix. The increase came from propagation and opening of micro-cracks, which were produced during the tetragonal to monoclinic

4

lattice transformation of ZrO_2. Later, Pohanka et al. (1978) studied the effect of phase transformation on the fracture behavior of $BaTiO_3$. A detailed mechanics explanation for transformation toughening was given by McMeeking and Evans (1982).

Secondary phase toughening, one of the major toughening mechanisms for high strength alloys, has also been employed to make tough ceramics. Kleebe et al. (1999) studied the influence of grain morphology and secondary phase chemistry on the fracture toughness of Si_3N_4 ceramics. Later, Yang and Chen (2000) incorporated a piezoelectric secondary phase $(Nd_2Ti_2O_7)$ in the Al_2O_3 ceramic and found the fracture of $Nd_2Ti_2O_7/Al_2O_3$ composite ceramic was significantly higher than single phase Al_2O_3 ceramic. In the work of Zhao et al. (2004), the fracture toughness of a diamond-SiC composite was found to be greatly enhanced due to the presence of the secondary diamond phase.

Microcracking is a well understood toughening mechanism that goes back to the work of Shum and Hutchinson (1990). They discovered that optimal toughening depends on the macrocrack/microcrack configuration that minimizes the maximum energy release rate among various crack tips. Depending on the specific material system, micro-cracks may come from phase transformation (Claussen 1976), or incorporation of a secondary phase (Evans and Faber 1981).

Toughening by weak interfaces includes a wide range of material systems. Clegg et al. (1990) produced silicon carbide (SiC) with graphite as weak interfaces and discovered that fracture toughness in the direction normal to the weak interfaces was increased more than fourfold compared to monolithic silicon carbide. The strengthening was claimed to be caused by crack deflection or branching at the interfaces. The effect of crack deflection on

fracture toughness was also investigated by Blanks et al. (1998), Ma et al. (2004), and Leguillon et al. (2006), successively. More recently, Reddy et al. (2012) explored the combined effect of nanoporosity and interfaces on the mechanical properties of nanoporous boron carbide (B_4C) and concluded that its compressive strength, plasticity and toughness can be increased by deformation-induced elimination of nanoporosity.

All ceramics and CMCs are heterogeneous to some extent. In transformation or secondary phase toughening, matrices and functioning constituents have different moduli. Ceramics with weak interfaces or laminate structures are heterogeneous by design; and nanoporosity in ceramics may be considered as extreme heterogeneity — the modulus of nanopores is zero. The study on the toughening mechanism of ceramics and CMCs not only provided guidance for the development of new ceramic materials that are both stiff and tough, but also laid foundation for related studies on materials with similar heterogeneous microstructures.

The other field of research on bridging the microstructure to overall fracture properties in heterogeneous material systems is driven by natural composites with superior fracture resistance, such as bones, nacre, and teeth (Gao et al. 2003, Fratzl and Weinkamer 2007, Meyers et al. 2008). These materials often have hierarchical structures spanning multiple length scales, resulting in enhanced mechanical properties far beyond their constituent materials.

In the work of Yao et al. (2013), it is found that crack-induced stress intensification in nacreous composites can be greatly suppressed due to a synergistic match of the mechanical properties between the two phases of a brick-and-mortar structure. The same hierarchical structures were also found in bones and teeth. Koester et al. (2008) used in-

situ mechanical testing to examine crack propagation in both transverse (breaking) and longitudinal (splitting) orientations in cortical bones. They concluded that crack resistance in the transverse direction is much large than in the longitudinal direction because of crack deflections. Bechtle et al. (2010) investigated crack propagation and arrest within the dentinoenamel junction region in teeth. They observed that a tooth sample would fracture after elastic and some amount of plastic deformation if cracks were induced from the dentin side. Results of stress intensities around crack tips were found to be greatly influenced by elastic modulus mismatch between the enamel and the dentin.

Besides the above-mentioned experimental investigations on ceramics and natural composites, research efforts on heterogeneous fracture also include analytical and computational modeling, which attempts to establish the relationships between the microstructure and macroscopic fracture properties in heterogeneous media.

Based on the Bueckner-Rice weight function theory (Bueckner 1987), Gao (1991) developed a first-order moduli-perturbation approach to analyze the fracture of nonhomogeneous materials. Later, Muju et al. (1998) extended this theory to a three-dimensional framework. Meanwhile, Bower and Ortiz (1991) studied crack propagation through a brittle matrix material with a regular distribution of tough particles. Three major mechanisms of fracture toughening were proposed in their work: distributed microcracking, crack trapping by tough grains, and frictional energy dissipation as grains are pulled out in the wake of the crack. Biner and Hu (2009) used a phase-field model to simulate the damage evolution in composites and demonstrated the reinforcement effects in discontinuously reinforced and laminated composites. In the work of Zheng and Shen (2010), a phase-field model was employed to study the shear band formation and crack

propagation in fiber-reinforced bulk metallic glasses. More recently, Li and Zhou (Li and Zhou 2013, Li and Zhou 2013) used both numerical simulations and analytical models to establish the correlation between the fracture toughness and microstructure in ceramic composites. They successfully developed the framework for evaluating fracture toughness through explicit simulations and analytical calculations.

The analytical and computational modeling of heterogeneous fracture covers a broad range of topics. Recent research efforts in this area have been heavily focused on the effects of elastic modulus mismatch on fracture. The role of modulus mismatch was highlighted in the insightful work of Fratzl et al. (2007). They analyzed the driving force for crack propagation inside a material where the Young's modulus varies periodically. It was shown that an effective crack stopping occurs when the ratio of elastic moduli is larger than about five. Later, Murali et al. (2011) developed a phase field method to study the role of modulus mismatch in layered, bioinspired composites. They found that a crack is arrested and may bifurcate when the crack goes from the stiff matrix to the soft layer, which leads to a significantly higher toughness compared to that of the matrix. Recently, Leguillon and Martin (Leguillon and Martin 2013, Leguillon and Martin 2013) used a coupled criterion (Leguillon 2002) to quantify the strengthening effect caused by the elastic contrast in layered structures. Two mechanisms of crack propagation, "step over" and "jump through", were proposed depending on the different modulus mismatch ratios of the two constituent materials.

Besides the research efforts to understand fracture behaviors of ceramics and natural composites, attempts are also made to mimic the hierarchal structures through artificial material systems. A pioneering work in this area was done by Munch et al. (2008).

Combining aluminum oxide and polymethyl methacrylate into ice-templated structures, they were able to produce hybrid materials with 'brick-and-mortar' structures similar to natural composites such as nacre and achieve a fracture toughness 300 times (in energy terms) that of the constituents and a yield strength comparable to those of aluminum alloys. With the aid of scanning electron microscopy, a confluence of toughening mechanisms, such as microcracks and uncracked-ligament bridging, was identified. In a more recent work, Gonzalez and Lambros (2013) performance both experiments and simulations to study crack path selection in polymers with inhomogeneous microstructures. They were able to produce inhomogeneous grain patterns with Young's modulus varying from 150 MPa to 208 MPa, by controlling the time of UV irradiation for different regions of the specimen. It was shown that crack initiation and growth processes in the specimen were sensitive to the applied load and local microstructure.

While these researchers have successfully fabricated heterogeneous materials, the role of elastic contrast in fracture toughening was not thoroughly understood. Two constituents of the hybrid material in the work of Munch et al. (2008) obviously have distinct elastic properties. However, the relationship between the modulus mismatch and the superior toughness of the composite were not investigated. In the work of Gonzalez and Lambros (2013), the emphasis was the mechanism of crack path selection, with very little information on the effective fracture toughness of their model materials. Moreover, the modulus mismatch ratios in these inhomogeneous polymers were not significant enough.

2.2 Additive Manufacturing of Heterogeneous Materials

Additive manufacturing (AM), sometimes referred to as three-dimensional printing, direct digital manufacturing, solid freeform fabrication, or rapid prototyping, is a general term to describe the technologies that build 3D objects by adding layer-upon-layer of material with information from a CAD file. Representative AM technologies currently available include stereolithography (SL) (Hull 1986), fused deposition modeling (FDM), selective laser sintering (SLS), electron beam melting (EBM), laser engineered net shaping (LENS), laminated object manufacturing (LOM), PolyJet and so on (Kruth 1991, Sachs et al. 1993, Yan and Gu 1996, Kruth et al. 1998, Wong and Hernandez 2012). Additive manufacturing has been widely used in areas such as light-weighed machines (Bletzinger and Ramm 2001), architectural models (Gibson et al. 2002), and medical models (Salmi et al. 2013) .

Stereolithography, developed by Hull (1986), is a process of generating three-dimensional objects by layer-upon-layer cure of a photopolymer resin with laser. Compared with other AM techniques, SL has advantages such as low capital cost, effective controlling of material properties, high accuracy and resolution (Melchels et al. 2010). Available as the earliest AM process, SL is still popular and versatile with broad applications in biomedical engineering (Melchels et al. 2010), ceramics (Griffith and Halloran 1996), electronics (Farnworth 2003), and microfabrication (Zhang et al. 1999).

AM technologies, initially used to fabricate homogeneous polymeric materials, later extended to other engineering materials like ceramics, metals, and composites (Kumar and Kruth 2010). Using AM technologies to make composite materials with heterogeneous properties not only improves the quality of products, but also increases efficiency. The

existing AM technologies of making composites generally fall into two categories — single-material method and multiple-material method.

In the single-material method, several different materials, liquid or solid, are mixed to form a single material system before manufacturing. The material systems may encompass constituents of the desired composite material and other assistive material for maintaining the shape of the composite or facilitating the manufacturing process. For example, SLS with mixed powder has been used to produce polymer matrix composites (Wiria et al. 2007). Zhang et al. (2001) fabricated a TiC-Ni functionally gradient materials (FGM) using LOM and combustion synthesis, where mixed power of Ti, C, and Ni was used to form FGM green parts before combustion. Greer et al. (1996) used SL to fabricate fiber-reinforced composites, where fibers were added in situ to the resin to get a composite structure. Other AM technologies, such as FDM (Masood and Song 2004) and LENS (Banerjee et al. 2004), were also utilized to fabricate composite materials with the single-material method. The single-material method maintains the architecture of the conventional AM systems, and can fabricate a wide variety of composites by simply changing the raw material. While this method has such advantages and is implemented in many applications, it has limitations such as inability to precisely design and control the material microstructure.

The idea of the multiple-material method has already drew the attentions of many researchers (Choi et al. 2011). In this method, the AM system is able to handle and process two or more different raw materials separately. Different materials are built into the final object successively or simultaneously without contaminating each other before fabrication.

Unlike the single-material method, the multiple-material method requires more refit of the original AM system.

Some of the attempts to build multi-material AM systems are based on the FDM technology. Jafari et al. (2000) successfully developed a system for fabrication of multiple ceramic actuators and sensors by modifying the traditional FDM system. Khalil et al. (2005) used a multi-nozzle biopolymer deposition system to construct tissue scaffolds. SLS is also a feasible technology for fabricating heterogeneous materials. Previous work (Jackson et al. 2000, Liew et al. 2001, Liew et al. 2002, Santosa et al. 2002) showed that SLS can be used to fabricate objects with specific distribution of heterogeneities. However, design of the material feeding and recoating system in SLS has limited its application in building composites with more complicated microstructures.

Currently, the only multi-material AM system in the market is the Objet Connex 3D printers (Stratasys Ltd., Eden Prairie, MN, USA). These printers use the PolyJet 3D printing technology. With inkjet heads, PolyJet 3D printers jet layers of photoactive resin onto a build tray and cure them with UV light. The layers build up one at a time to create a 3D object. Compared with other AM processes, the PolyJet 3D printing technology offers many benefits such as superior quality and speed, high precision, and a very wide variety of materials. However, PolyJet 3D printing can only use jettable liquid materials, which limit the fabrication from more viscous liquid materials and eventually limits the material properties that the final product can achieve.

By modifying the commercial apparatus, stereolithography is also employed to fabricate composite materials. Wicker's research group developed a multi-material stereolithography (MMSL) machine (Wicker et al. 2004, Wicker et al. 2009, Choi et al.

2011). The MMSL machine was successfully applies to areas including tissue engineering (Choi et al. 2010) and micro-stereo-lithography (Arcaute et al. 2006, Arcaute et al. 2010). More recently, Chan et al. (2012) used a similar technology to fabricate hydrogel cantilevers and actuators for biohybrid applications.

The additive manufacturing system developed in the present work is a simplified stereolithography apparatus using the multiple-material method. Generally, the commercial 3D printers can only build materials with similar elastic properties — typically a modulus mismatch within 1:2 in order to have good interfacial bonding. With the 3D printer developed in this thesis, the two materials can have dramatically different properties while retaining good interfacial properties. Therefore, the mechanical properties of as-fabricated specimens can be precisely controlled over a wide range. The other innovation with this system is the use of Fresnel and parallel illumination, which overcomes the drawback of the existing stereolithography systems such as laser shadow and trapped volume (Choi et al. 2011).

Despite the various advantages offered by this novel system, there are still some issues to be addressed. First, we only focused on fabrication of heterogeneous materials with uniform pattern throughout the entire thickness. In order to build objects with more complex geometry, a control system is needed to process slice information (STL file) of the desired object and send out corresponding images for projection. Another issue is the lack of a recoating system. In addition, specimens printed using this printer may contain some defects. One of the noticeable defects is the specimen warpage and delamination from the printing platform, which is resulted from the residual stress induced by polymerization

shrinkage. By roughening the printing platform and adding a rectangle base layer, this defect can be largely eliminated.

2.3   Significance of the Current Research

In this thesis, a combined experimental and modeling effort is made to investigate the fracture behaviors of a heterogeneous material. From the numerical simulation results, it is concluded that the mismatch of elastic modulus has a tremendous impact on the material's effective fracture properties. Substantial enhancement in the fracture toughness can be achieved using carefully tuned material and geometrical parameters. The fracture mechanisms under different parameters are further examined through a comprehensive parameter study. In the experimental part, heterogeneous specimens are fabricated using a novel additive manufacturing setup and fracture tested by the tapered double-cantilever-beam (TDCB) approach. The effective fracture properties of the heterogeneous materials and the role of modulus mismatch are further investigated experimentally. The experimental results reveal that heterogeneous TDCB specimens with optimized material and geometrical parameters exhibit higher fracture toughness than their homogenous counterparts, which is in good agreement with the computational predictions. To sum up, the integrative computational and experimental study presented here provides a fundamental mechanistic understanding of the fracture mechanisms in brittle heterogeneous materials and sheds light on the rational design of ultra-tough materials through patterned heterogeneities.

CHAPTER 3

COMPUTATIONAL MODELING OF FRACTURE IN

HETEROGENEOUS MEDIA

3.1 Problem Definition

The problem of interest is illustrated in Figure 1. An infinite heterogeneous planar medium is subject to a remote K_I^∞ and T-stress field. The planar medium consists of two isotropic elastic materials with different elastic moduli, resulting in a patterned Young's modulus distribution varying with a period of p. The volume fraction of the stiff material is denoted by λ. The two materials differ in their Young's moduli, with all other mechanical properties, including intrinsic fracture toughness and Poisson's ratios, kept the same. An initial crack is placed at the center of the plane. The area away from the crack tip is modeled as a homogenized region with anisotropic material properties. With a fixed T-stress field, the crack propagates along the predefined path once K_I^∞ reaches a critical value. The crack propagation is modeled using a cohesive zone approach.

The fracture resistance curve is obtained by recording the applied far-field stress intensity factor and measuring the corresponding crack extension. Due to the periodicity of the problem, the crack is only allowed to extend for one period of length. In this model, the overall compliance of the system is maintained regardless of the crack tip position. Thus, the fracture behavior within one period is enough to characterize the whole system. This model is similar to the one used in Fratzl et al. (2007)'s work, where the variation of Young's modulus was characterized by a cosine function.
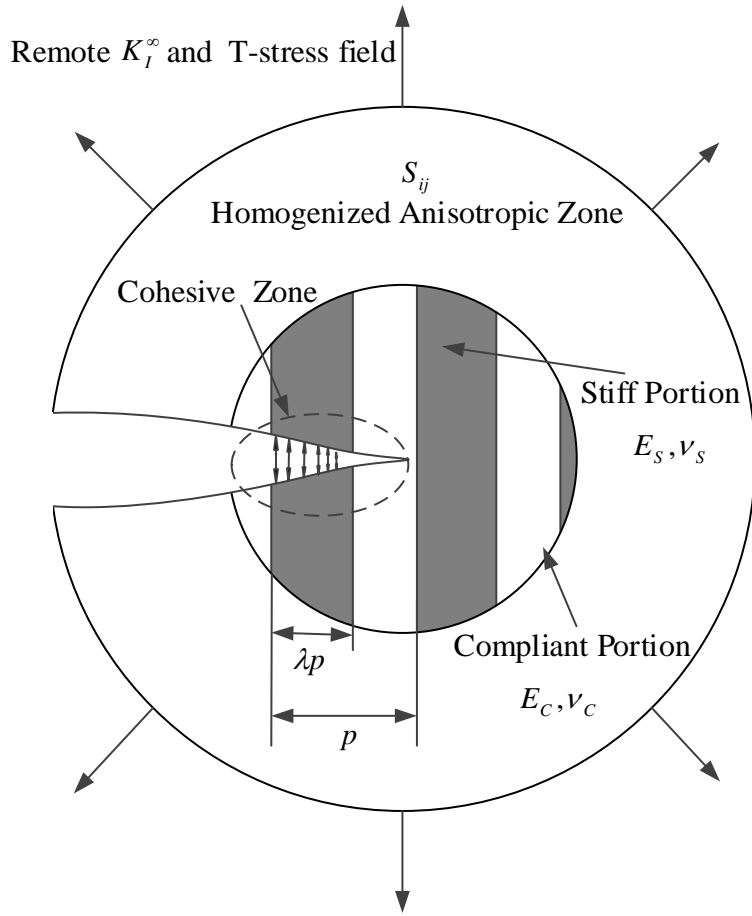
Figure 1. Schematic of a semi-infinite crack growing within an infinite heterogeneous medium. Stiff and compliant portions of the plane are organized in a laminate structure with period p. The volume fraction of the stiff material is denoted by λ. E_S, ν_S, E_C, ν_C represent the Young's moduli and Poisson's ratios of the two constituents. The area away from the crack tip is modeled as a homogenized anisotropic region with an elastic compliance matrix S_{ij}. The crack propagation is modeled using a cohesive zone approach. The whole system is subjected to a combined K_I^∞ and T-stress loading in the far field. Note that the figure is not drawn to scale.

3.2　Finite Element Model

The problem stated in Section 3.1 is solved numerically using finite element analysis with plane stress assumptions. Due to geometrical and loading symmetry about the crack plane, only the upper half is modeled for the sake of computational efficiency.

The infinitely large plane is modeled as a semi-circular disc of diameter 2000 mm. The laminated semi-circular region has a diameter of 100 mm. The spatial period of the material heterogeneity, $p = 10$ mm, is fixed for all simulations. The volume fraction of the stiff material (λ) varies from 0.1 to 0.9. Young's moduli of the two materials in the laminated region are E_S for the stiff material, and E_C for the compliant material. The Poisson's ratios for the stiff and compliant materials are v_S and v_S, respectively. To simplify the problem, $v_S = v_C = 0.3$ and $E_C = 100$ MPa remain unchanged for all simulations in this chapter (Chapter 3). E_s is made to vary from 100 MPa to 600 MPa. The anisotropic elastic properties assigned to the semi-annular homogeneous anisotropic zone are the effective values calculated based on the elastic properties and orientations of the two constituents. The compliance matrix S_{ij} for the homogenized zone is given by the following equation:

$$S_{ij} = \begin{bmatrix} 1/E_{11} & -v_{21}/E_{22} & -v_{31}/E_{22} & 0 & 0 & 0 \\ -v_{12}/E_{11} & 1/E_{22} & -v_{32}/E_{22} & 0 & 0 & 0 \\ -v_{13}/E_{11} & -v_{23}/E_{22} & 1/E_{22} & 0 & 0 & 0 \\ 0 & 0 & 0 & 1/G_{23} & 0 & 0 \\ 0 & 0 & 0 & 0 & 1/G_{13} & 0 \\ 0 & 0 & 0 & 0 & 0 & 1/G_{12} \end{bmatrix} \tag{1}$$

where E_{ij}, v_{ij}, G_{ij} are elastic constants calculated from E_S, E_C, v_S, v_C, and λ. The detailed derivation of this matrix is presented in Appendix A.

During crack growth, a fracture process zone will occur ahead of the crack tip. In the finite element model, the fracture process zone is defined at the interface between the upper plane and the imaginary lower plane. The behavior of this interface is modeled using a cohesive traction-separation law that relates the normal and tangential displacements

17

(δ_n, δ_t) and the normal and tangential tractions (σ_n, σ_t). In this work, a bi-linear constitutive law (Repetto et al. 2000) is used to simulate crack initiation and propagation. To solve the numerical convergence problem, an artificial viscosity term (Gao and Bower 2004) is added in the constitutive equations. The combination of bi-linear constitutive law and artificial viscosity term was first implemented by Xia et al. (2007). The corresponding equations for the normal and shear tractions are presented as below:

$$\sigma_n = \begin{cases} \sigma(\delta)\dfrac{\delta_n}{\delta} + \zeta\dfrac{\dot{\delta}_n}{\delta_C}, & \delta_n > 0 \\[4mm] k_C\delta_n + \zeta\dfrac{\dot{\delta}_n}{\delta_C}, & \delta_n < 0 \end{cases} \tag{2}$$

$$\sigma_t = \begin{cases} \sigma(\delta)\dfrac{\beta^2\delta_t}{\delta} + \zeta\dfrac{\dot{\delta}_t}{\delta_C}, & \delta_n > 0 \\[4mm] \sigma(\beta\delta_t)\beta\,\mathrm{sgn}(\delta_t) + \zeta\dfrac{\dot{\delta}_t}{\delta_C}, & \delta_n < 0 \end{cases} \tag{3}$$

where $\delta = \sqrt{\delta_n^2 + \beta^2\delta_t^2}$ is an effective opening displacement, β is a parameter controlling the weights of the normal and shear opening displacements, k_C is a contact stiffness used for resisting interfacial inter-penetration, and ζ is a coefficient of fictitious viscosity. The relationship between σ and δ is given in Figure 2.

The bi-linear traction-separation law is characterized by three key parameters. σ_m is the maximum traction, δ_m is the separation corresponds to σ_m, and δ_C is the separation beyond which the traction drops to zero. The cohesive zone model is
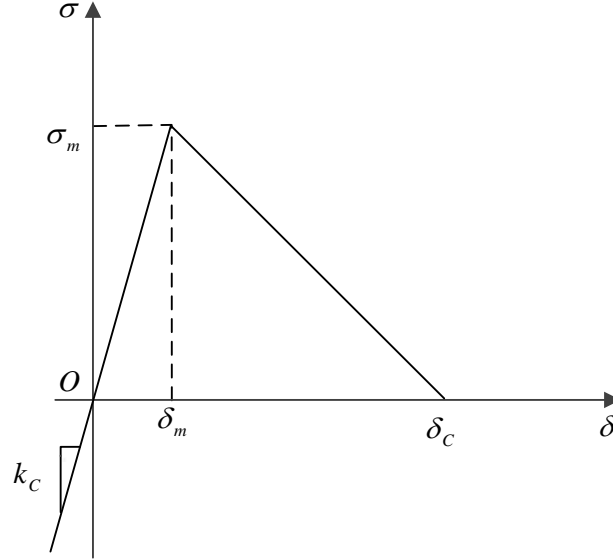
Figure 2. $\sigma - \delta$ relation for a bilinear traction-separation law.

implemented in Abaqus 6.12 with the user element subroutine (UEL). The nodal forces and stiffness matrices computed for the cohesive zone elements are assembled with the rest of the internal force vectors and stiffness matrices to form a global stiffness matrix and load vector. The problem in the present work is modelled as pure Mode I fracture. Therefore, we only need to consider normal traction and opening displacement components. For all the simulations in this thesis, the following parameters are kept constant: $\delta_m / \delta_C = 0.01$, $k_C = 10^6$ MPa/mm, $\zeta = 10^{-6}$.

The analysis presented in this chapter is performed using the finite deformation theory. Quasi-static condition and negligible body forces are assumed for all simulations. Using this finite element model, the effects of various material and geometrical parameters on the material's fracture behavior are explored, including the modulus mismatch ratio, phase volume fractions, T-stress, and cohesive zone size.

3.3 Instability Control Algorithm

Snap-back instability, i.e. the simultaneous reduction of the load and displacement at a critical load point, is often observed in the fracture tests of heterogeneous materials (Bocca and Carpinteri 1990, Bosco et al. 1990). For computational modeling of fracture, the snap-back instability can be overcome by introducing artificial viscous energy dissipation. However, this method is not able to capture the real path of unstable crack growth. Moreover, the fracture toughness calculated with this method is usually higher than the true value when snap-back instability occurs. Displacement-controlled or load-controlled boundary conditions are most commonly used in finite element analysis. However, neither of the two is capable of obtaining a complete load-displacement curve of unstable crack growth when the standard non-linear Newton-Raphson scheme is used. In order to overcome the snap-back instability and recover the complete load-displacement curve at the same time, one possible solution is to find a variable that increases monotonically during the entire loading process. Based on this criterion, Segurado and LLorca (2004) developed a crack-tip-opening controlled algorithm, in which the sum of the opening displacements of all interfacial elements along the predefined crack path is chosen as a loading parameter. Originally, this algorithm was implemented to simulate fracture in particle-reinforced composites. In this work, the crack-tip-opening controlled algorithm is modified and implemented to solve the snap-back instability problem in the 2D model of heterogeneous fracture. Detailed description of this method is presented as follows.

We first choose a node from an interfacial cohesive zone element. Denote the node number, displacement, and nodal force of this node in the y direction as N, u_2^N, P_2^N. Then, we create a dummy control node with a node number of C. The displacement of the control node in the y direction is u_2^C, and its nodal force in the y direction is P_2^C. This control node has no geometrical meaning and is only used for the purpose of instability control. For this control node, we specify $P_2^C = u_2^N$ and assemble this control node and the node N to form a virtual element. The stiffness matrix for this element can be expressed by Equation (4).

$$\begin{pmatrix} 0 & 0 \\ 1 & 0 \end{pmatrix} \begin{pmatrix} u_2^N \\ u_2^C \end{pmatrix} = \begin{pmatrix} P_2^N \\ P_2^C \end{pmatrix} \tag{4}$$

To relate the cohesive failure to the far-field loading, we construct another virtual element from the control node and a node that is located at the far-field boundary. The node number, displacements and nodal forces of the far-field node are denoted as L, u_1^L, u_2^L, P_1^L, P_2^L. The stiffness matrix for this element is defined in Equation (5):

$$\begin{pmatrix} 0 & 0 & f_1 \\ 0 & 0 & f_2 \\ 0 & 0 & 0 \end{pmatrix} \begin{pmatrix} u_1^L \\ u_2^L \\ u_2^C \end{pmatrix} = \begin{pmatrix} P_1^L \\ P_2^L \\ P_2^C \end{pmatrix} \tag{5}$$

where f_1, f_2 are the loading coefficients to be determined. The above equation establishes a relationship between the vertical displacement of the control node and the applied far-field load in the vertical and horizontal directions. The values of f_1 and f_2 are so define as to yield the following equality:

$$K_I^\infty = u_2^C \tag{6}$$

21

where K_I^∞ is the Mode I stress intensity factor in the far field. f_1 and f_2 are determined from the stress equations of a cracked anisotropic body under symmetric loading (Sih et al. 1965). The final expressions of f_1 and f_2 are as follows:

$$f_1 = \frac{A}{\sqrt{2\pi r}} \mathrm{Re}\left[\frac{\mu_1 \mu_2}{\mu_1 - \mu_2}\left(\frac{\mu_2}{\sqrt{\cos\theta + \mu_2 \sin\theta}} - \frac{\mu_1}{\sqrt{\cos\theta + \mu_1 \sin\theta}} \right)\right] \tag{7}$$

$$f_2 = \frac{A}{\sqrt{2\pi r}} \mathrm{Re}\left[\frac{1}{\mu_1 - \mu_2}\left(\frac{\mu_1}{\sqrt{\cos\theta + \mu_2 \sin\theta}} - \frac{\mu_2}{\sqrt{\cos\theta + \mu_1 \sin\theta}} \right)\right] \tag{8}$$

where $r,\ \theta$ are the polar coordinates, and A is the element size at the far-field boundary. μ_1, μ_2 are the material constants obtained by solving the following characteristic equation:

$$S_{11}\mu^4 - 2S_{16}\mu^3 + 2(S_{12} + S_{66})\mu^2 - 2S_{26}\mu + S_{22} = 0 \tag{9}$$

where S_{ij} is the compliance matrix representing the anisotropic material properties. μ_1, μ_2 are chosen as the roots of the above equation with positive imaginary part.

In the finite element analysis, the control node is connected to each of the surface nodes at the cohesive interface (where the cohesive zone law is defined), resulting in a group of 2-node elements. Similarly, the control node is also connected to each of the surface nodes at the far field (where the far-field stress is applied) to form another group of 2-node elements with stiffness matrices defined by Equation (5). The stiffness matrices of these virtual elements are then assembled into the global stiffness matrix of the model.

This stability control technique is implemented in Abaqus 6.12 with the user element subroutine (UEL). To run the program, a virtual force F, which is equal to the sum of displacements of all the cohesive zone nodes, is applied to the control node. When F

keeps increasing over time, the crack will initiate and propagate steadily. The stress intensity factor in the far field is obtained by recording the vertical displacement of the control node. By measuring the crack tip position at different time steps, a complete fracture resistance curve is constructed.

3.4   Representative Results

In this section, the fracture behaviors of several representative cases are presented and analyzed. Figure 3 shows a series of fracture resistance curves for three different modulus mismatch ratios. The T-stress is set to be zero in the three cases. Besides the fixed parameters that are specified in Section 3.2, $\lambda = 0.5$ and $\sigma_m / E_C = 0.1$, are also fixed for the three curves. The intrinsic critical energy release rates (CERR) of the stiff and compliant phases are the same: $\Gamma = 0.4$ KJ/m². The theoretical K_{IC} values for homogeneous isotropic materials with different moduli are calculated using: $K_{IC} = \sqrt{\Gamma E}$. The effective stress intensity factor for the homogenized anisotropic zone is calculated using the following equation (Banks-Sills et al. 2005):

$$K_I = \sqrt{\frac{\Gamma}{D_0 \sqrt{S_{22}}}}$$

(10)

where

$$D_0 = [2\sqrt{S_{11}S_{22}} + 2S_{12} + S_{66}]^{1/2}$$

(11)

In the two equations above, S_{ij} is the compliance matrix of the homogenized anisotropic zone. For each case, K_I^∞ values calculated for the homogeneous materials with elastic

23

properties of E_S and S_{ij} are compared with the simulation results. The modulus mismatch ratios used in the three cases are: $E_S / E_C = 1.5, 3.0, 6.0$, respectively. For all the fracture resistance curves presented in this chapter, the cohesive crack starts from a stiff-to-compliant interface. One period of crack growth is simulated for each case and duplicated to obtain the two-period results presented here.

In Figure 3a, a significant enhancement in fracture toughness is observed when comparing the simulation result with the critical stress intensity factors of the two homogneous materials. Remarkably, the peak value of K_I^∞ of the heterogeneous material is found to exceed the K_{IC} value of the stiff constituent. From the fracture resistance curve in Figure 3a, some common features of heterogeneous crack propagation can be identified. K_I^∞ starts from a relatively low value at the stiff-to-compliant interface, and keeps increasing as crack extends within the compliant region. When the crack tip is close to the compliant-to-stiff interface, the stress intensity factor increases sharply with very little crack extension. This indicates the crack arrest at the interface. Once the peak value of K_I^∞ is achieved at the compliant-to-stiff interface, K_I^∞ decreases dramatically as the crack propagates in the stiff region.
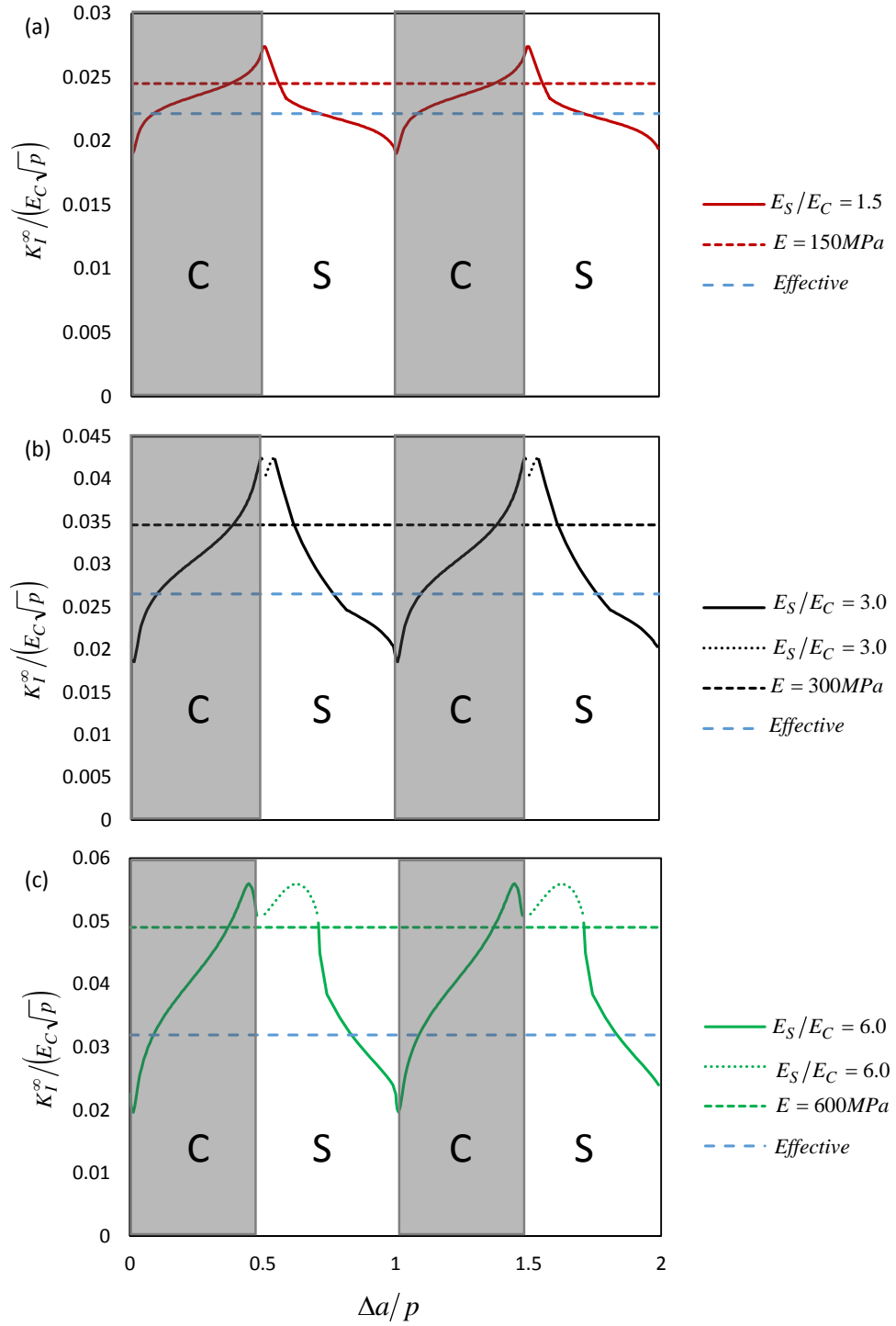
Figure 3. Representative results of fracture resistance curves with different modulus mismatch ratios. The two horizontal lines in each figure represent K_I^∞ values calculated for the homoneneous materials with elastic properties of E_s and S_{ij}, respectively. 'C' and 'S' indicte the compliant and stiff regions. In (b) or (c), the doted curve represents the extension of the secondary crack.
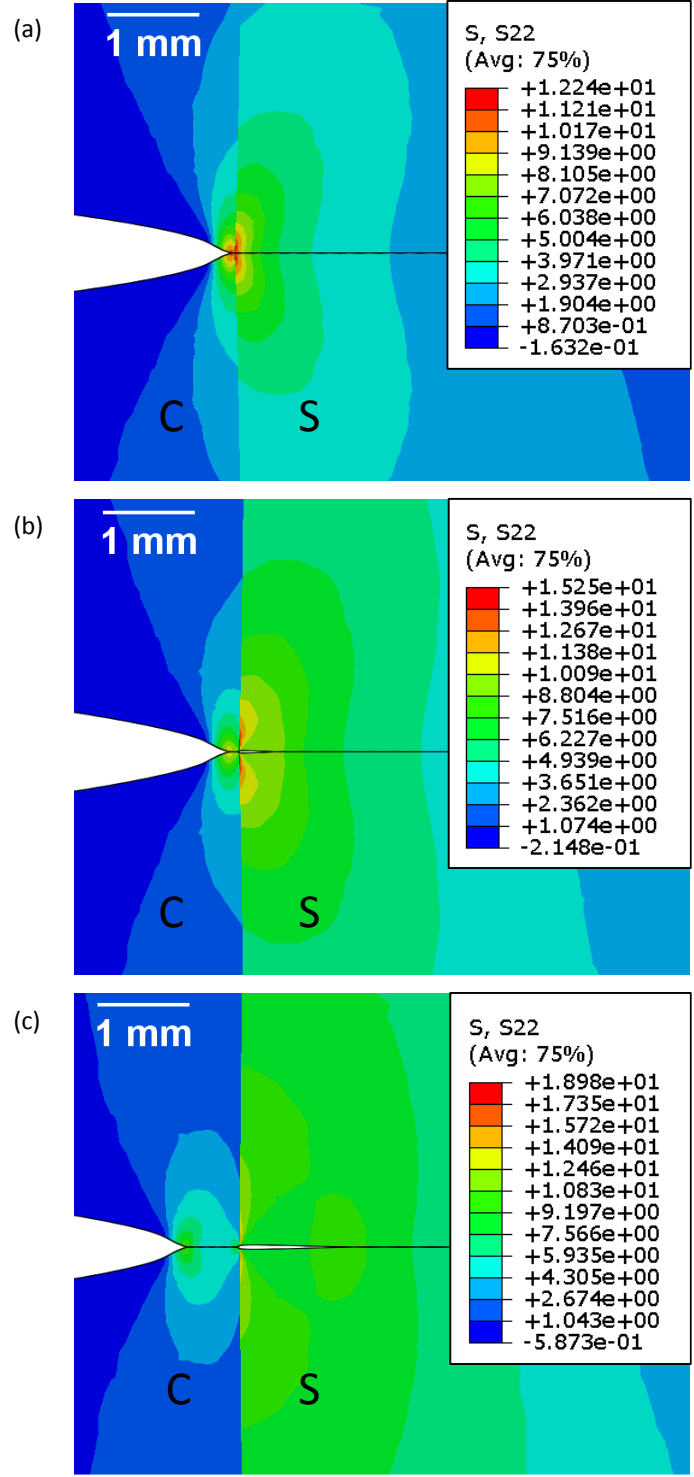
Figure 4. Stress contour plots of σ_{yy} for different modulus mismatch ratios. (a) $E_S / E_C = 1.5$, (b) $E_S / E_C = 3.0$, (c) $E_S / E_C = 6.0$. The snapshot in each case is taken at the first peak of the $K_I^{\infty} - a$ curve. Secondary cracks are observed in (b) and (c). Note that the deformation scale factors are set to be one and three in the x and y directions, respectively.

In the case of $E_S / E_C = 1.5$ (Figure 3a), the crack grows by continuous extension of

the original crack. When $E_S / E_C = 3.0$ or 6.0 (Figure 3b and 3c), the general trend of K_I^∞

variation is similar to the $E_S / E_C = 1.5$ case. However, sharp discontinuities and secondary

cracks are observed in the two cases with high mismatch ratios, as shown by the stress

contour plots in Figure 4. When the primary crack is close to the compliant-to-stiff interface,

a secondary crack is seen to initiate ahead of the primary crack and grow simultaneously

with the primary crack. At one critical point after reaching the peak K_I^∞, the two crack

fronts merge, resulting in a jump of the primary crack tip position.

Leguillon and Martin (2013) studied the strengthening effect caused by elastic

contract with theoretical calculations. They proposed two failure mechanisms "step-over"

(with secondary crack) and "jump-through" (no secondary crack). According to their

calculations, when the mismatch ratio (E_s / E_c) is large, the critical applied load at failure

for the "step-over" mechanism is smaller than for the "jump-through" mechanism. In other

words, when the mismatch ratio is large, the secondary crack is more likely to nucleate

before the primary crack reaches the interface. Our simulation results presented here

validate these two mechanisms.

3.5   Parametric Studies

In the present study, the key parameters that affect the effective fracture toughness

of heterogeneous materials include the geometrical parameters, material parameters,

cohesive zone parameters, and T-stress field. The geometrical parameters describe the

pattern and volume fractions of the two material constituents, including the spatial period of the material heterogeneity p and the stiff phase volume fraction λ. The material constants are the Young's Moduli, E_S, E_C, and the Poisson's ratios, ν_S, ν_C, of the two materials. The cohesive zone parameters include the critical energy release rate Γ and the maximum cohesive traction σ_m.

The far field Mode I stress intensity factor K_I^∞ can be expressed by the following function:

$$K_I^\infty = f(\Delta a, p, \lambda, E_S, E_C, \nu_S, \nu_C, \Gamma, \sigma_m, T) \tag{12}$$

With a dimensional analysis, the function of normalized K_I^∞ can be written in the following dimensionless form:

$$\frac{K_I^\infty}{E_C\sqrt{p}} = \Pi(\frac{\Delta a}{p}, \lambda, \frac{E_S}{E_C}, \nu_S, \nu_C, \frac{\Gamma}{pE_C}, \frac{\sigma_m}{E_C}, \frac{T}{E_C}) \tag{13}$$

As mentioned in Sections 3.2 and 3.4, $p = 10$ mm, $E_C = 100$ MPa, $\nu_C = \nu_s = 0.3$, and $\Gamma = 0.4$ KJ/m^2, are fixed. In the remainder of this chapter, the influence of $\lambda, \dfrac{E_S}{E_C}, \dfrac{\sigma_m}{E_C}$, and

$\dfrac{T}{E_C}$ on the fracture behaviors of heterogeneous materials is investigated.

Figure 5 shows the fracture resistance curves with different modulus mismatch ratios. It is obvious that the variation in the modulus mismatch ratio has a dramatic influence on the fracture toughness of the material system. With the same compliant constituent, a higher modulus mismatch ratio increases the effective fracture toughness. Compared with the fracture toughness values of the corresponding stiff constituents, all
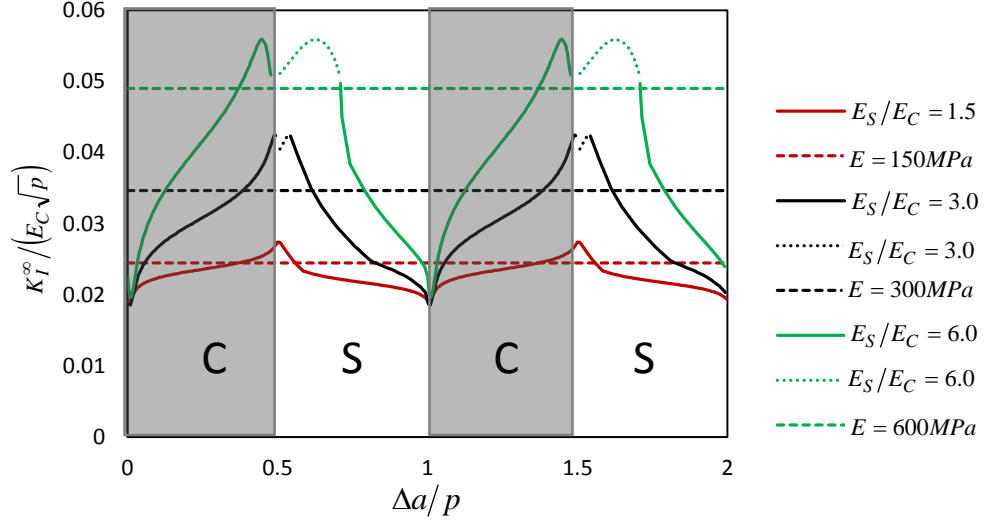
Figure 5. Fracture resistance curves with different modulus mismatch ratios E_s / E_c. Other parameters are: $\lambda = 0.5$, $\sigma_m / E_c = 0.1$, and T = 0. The three horizontal lines represent the homogeneous $K_I^\infty / (E_C \sqrt{p})$ values calculated from E_S = 150 MPa, E_S = 300 MPa, and E_S = 600 MPa, respectively.
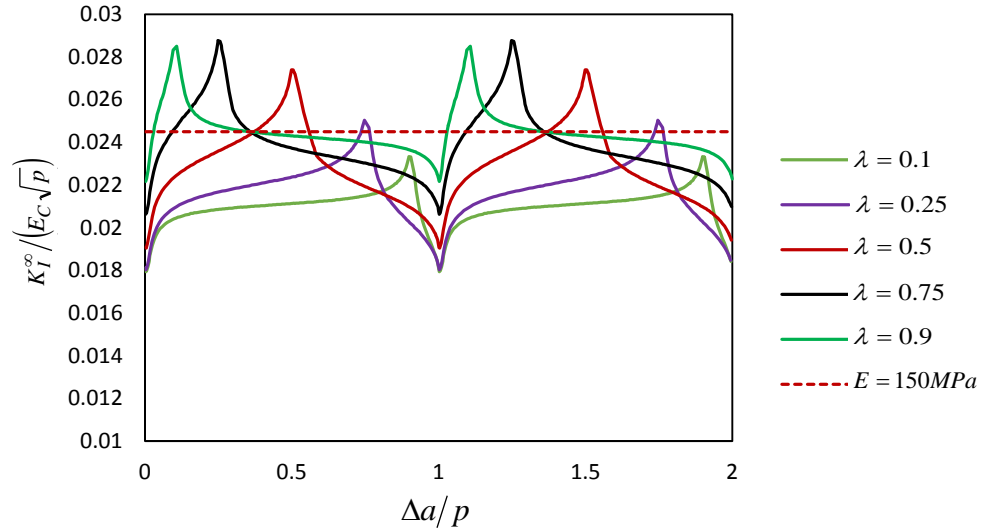
Figure 6. Fracture resistance curves with varying stiff volume fractions λ. Other parameters are $E_S / E_C = 1.5$, $\sigma_m / E_C = 0.1$, and T = 0. The two horizontal lines represent the homogeneous $K_I^\infty / (E_C \sqrt{p})$ values calculated from E_S and S_{ij}, respectively.

the three heterogeneous material systems exhibit substantial enhancement in their effective fracture toughness. As the modulus of the stiff constituent increases, the overall rigidity of the material system also increases simply by the rule of mixture, resulting in larger load required to initiate and extend the crack. Meanwhile, with a higher modulus mismatch ratio, the crack arrest at a compliant-to-stiff interface will be more severe and the energy required for the crack to pass the interface is higher.

The influence of the stiff phase volume fraction λ on the fracture behaviors of heterogeneous materials is illustrated in Figure 6. Compared with the fracture toughness of the homogeneous stiff material, the heterogeneous material system exhibits noticeable enhancement in fracture toughness when $\lambda \geq 0.25$. The highest possible fracture toughness is achieved with an optimal volume fraction near $\lambda = 0.75$. When the stiff phase volume fraction is below the optimal λ value, the fracture toughness of the heterogeneous material will increase as λ increases. Beyond the optimal λ value, the fracture toughness will decrease as λ further increases.

When λ is within a modest range, the overall rigidity of the materials system will increase as the stiff phase volume fraction increases. A higher rigidity will increase the force required to initiate and grow the crack, resulting in higher fracture toughness. However, when one of the constituent materials, whether stiff or compliant, dominants the material system, the fracture behavior of the system tends to be close to the dominant material. The enhancement due to crack arrest and modulus mismatch will decrease dramatically as the volume fraction of one phase further increases. This explains the fluctuations in the fracture resistance curves with different stiff phase volume fractions.
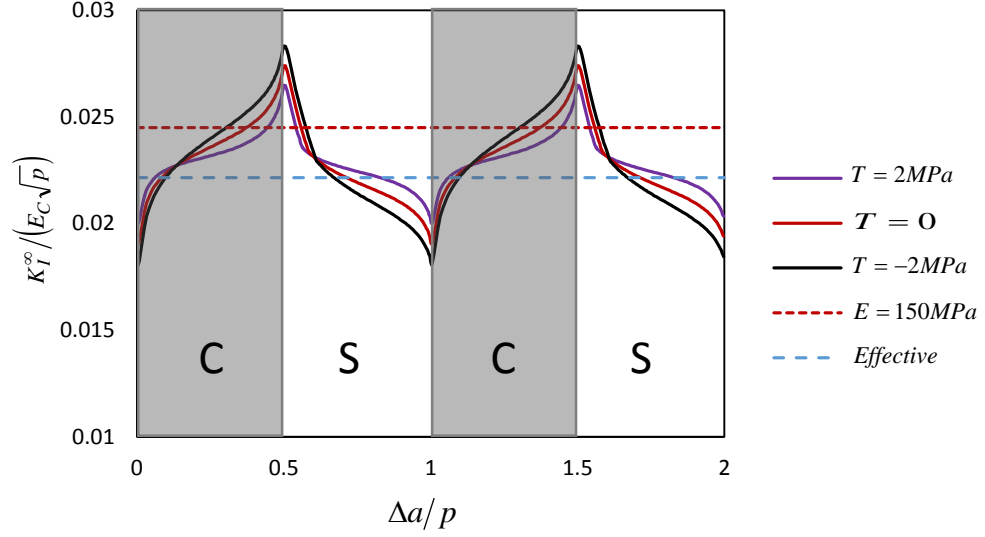
Figure 7. Fracture resistance curves with different T-stress fields. Other parameters are $\lambda = 0.5$, $E_S/E_C = 1.5$, and $\sigma_m/E_C = 0.1$. The two horizontal lines represent the homogeneous $K_I^\infty/(E_C\sqrt{p})$ values calculated from E_S and S_{ij}, respectively.
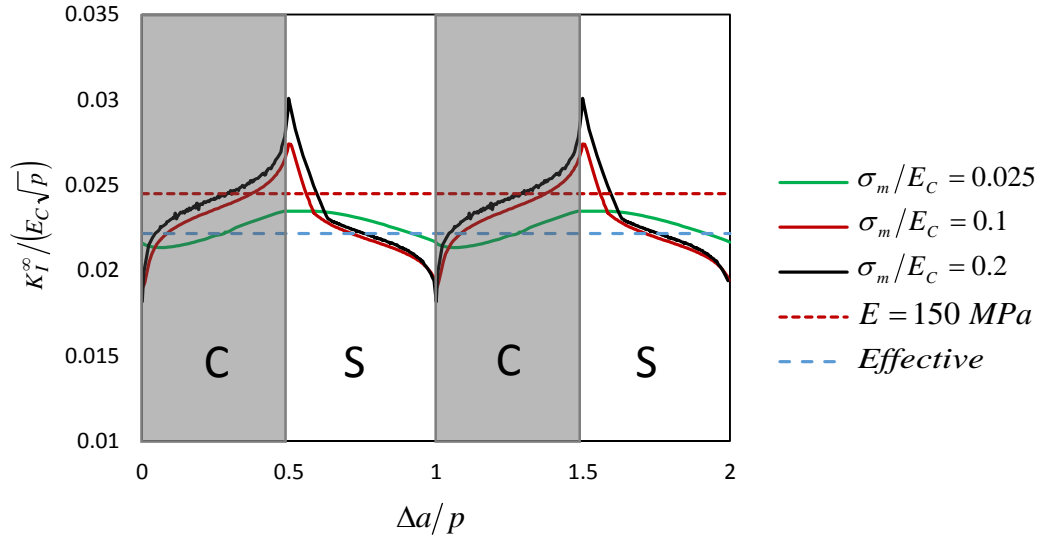
Figure 8. Fracture resistance curves with different cohesive zone parameters σ_m/E_c. Other parameters are: $\lambda = 0.5$, $E_S/E_C = 1.5$, and T = 0. The two horizontal lines represent the homogeneous $K_I^\infty/(E_C\sqrt{p})$ values calculated from E_S and S_{ij}, respectively.
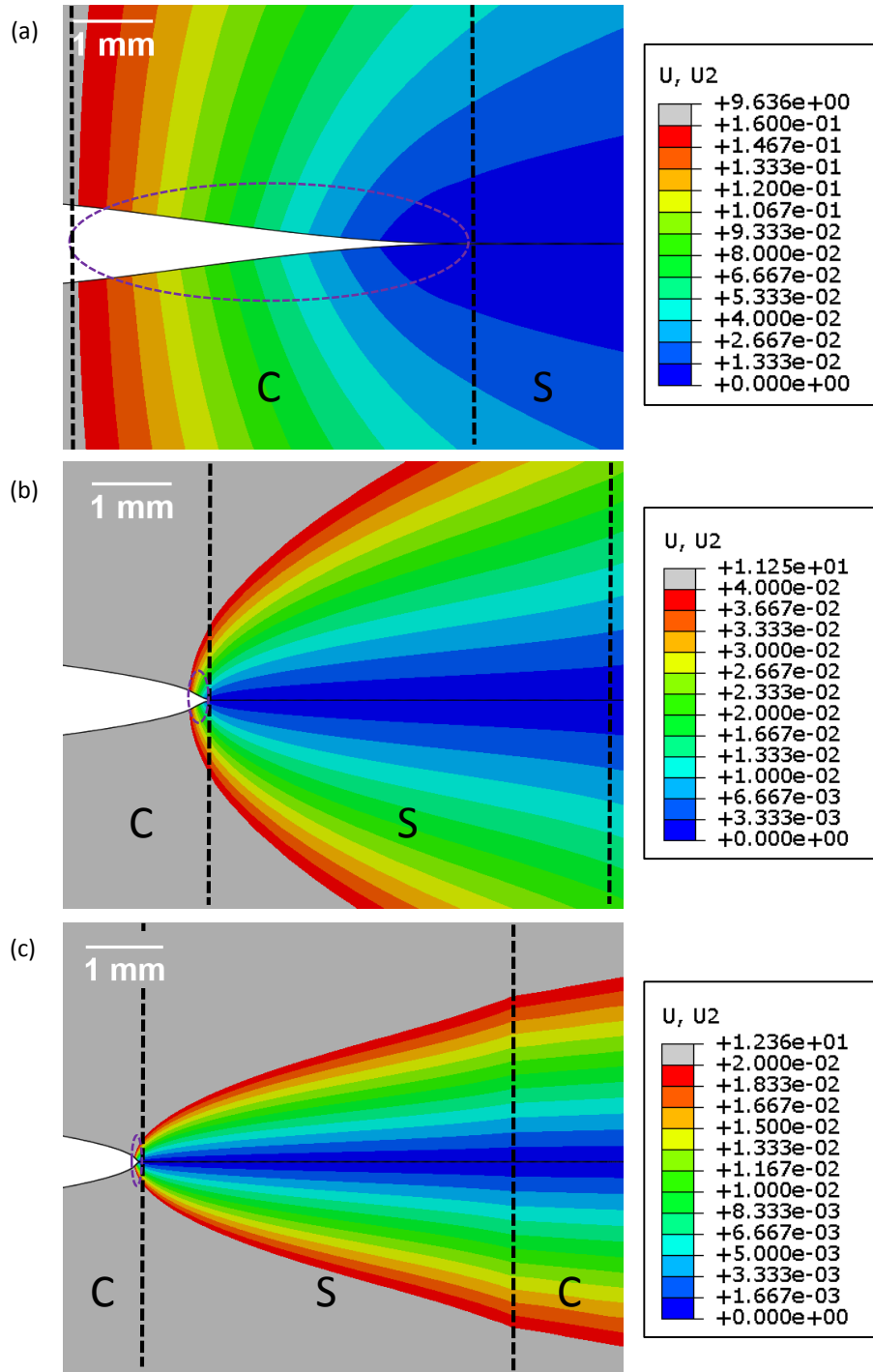
Figure 9. Displacement contour plots of U_2 with different cohesive zone parameters. (a) σ_m / E_C = 0.025, (b) $\sigma_m / E_C = 0.1$, (c) $\sigma_m / E_C = 0.2$. Other parameters are: $\lambda = 0.5$, $E_S / E_C = 1.5$, and T = 0. The doted circles indicate the cohesive zones. Note that the deformation scale factors are set to be one and three in the x and y directions, respectively.

T-stress is another important parameter that affects the fracture behaviors of heterogeneous material systems. The fracture resistance curves with three different T-stress fields are illustrated in Figure 7. In the present work, tensile T-stresses are denoted as positive. It can be seen that, a positive T-stress reduces the effective fracture toughness, while a negative T-stress increases it. The observed T-stress effect is due to the fact that a negative T-stress tends to close the crack at the compliant-to-stiff interface, which increases the remote K_I^∞ value for crack propagation.

The fracture resistance curves with three different cohesive zone parameters σ_m / E_C are presented in Figure 8. With the same critical energy release rate, the heterogeneous material systems exhibit higher fracture toughness than the homogeneous materials with effective elastic properties. However, in $\sigma_m / E_C = 0.025$ case, the enhancement is minimal and the peak value of heterogeneous fracture toughness does not exceed that of the stiff component.

The above results can be explained by the difference in the cohesive zone sizes of the three material systems, as shown in Figure 9. The cohesive zone is identified as the interfacial region with opening displacement less than $\delta_m / 2$ in each case. The three snapshots are taken at the peak K_I^∞ when the crack front is near the compliant-to-stiff interface. Since $\Gamma = \sigma_m \delta_c / 2$ is kept constant, the influence of σ_m actually comes from the corresponding variation in δ_c, which is directly related to the cohesive zone size. In the $\sigma_m / E_C = 0.025$ case, the cohesive zone size is large and comparable to the characteristic length of the material heterogeneity (i.e., the spatial period of the elastic heterogeneity p).

Therefore, the simulated $K_I^\infty - a$ curve in this case approaches the value of a homogeneous material with an effective elastic modulus. However, when $\sigma_m / E_C = 0.1$ or 0.2, the cohesive zone size is small when compared with the characteristic length, thus leading to a great enhancement in the effective fracture toughness.

3.6 Conclusions

Computational modeling of crack propagation in a heterogeneous planar medium is performed using Abaqus finite element analysis with the user element subroutine UEL. Two control algorithms are implemented to address the challenges in convergence and instability control. The combination of a bilinear cohesive zone law and artificial viscous energy dissipation solves the convergence problem. A crack-tip-opening controlled algorithm is implemented to overcome the instability problems associated with inherently unstable crack growth. Computational results indicate that the mismatch of elastic modulus is an important factor in determining the fracture behaviors of the heterogeneous model material. Significant enhancement in the material's effective fracture toughness can be achieved with appropriate modulus mismatch.

Systematic parametric studies are also performed to investigate the effects of various material and geometrical parameters, including the modulus mismatch ratio, the stiff phase volume fractions, the T-stress field, and the cohesive zone parameters. Conclusions from the parametric study are summarized as below:

1) A large modulus mismatch ratio leads to high effective fracture toughness and severe crack instability in heterogeneous material systems.

2) For given constituent materials, there exists an optimal value for the stiff phase volume fraction which yields maximum enhancement in fracture toughness.

3) T-stress is an important factor that affects the effective fracture toughness of heterogeneous materials. A negative T-stress field helps to increase the fracture toughness.

4) The cohesive zone parameters have a significant impact on the fracture toughness of heterogeneous materials. When the cohesive zone size is comparable to the characteristic length of material heterogeneity, the enhancement in fracture toughness becomes negligible.

The numerical results presented in this chapter are effective tools for guiding experimental investigations and predicting the fracture behaviors of heterogeneous materials.

CHAPTER 4

FRACTURE TESTS OF HETEROGENEOUS MATERIALS

4.1   Additive Manufacturing System

In the current research, a novel additive manufacturing system is developed and used for fabricating heterogeneous test specimens with well-controlled structural and material properties. This additive manufacturing system is based on the stereolithography (SL) technology. Using the multiple-material method, it is capable of building different materials with distinct mechanical properties within one object. A schematic drawing and a photograph of the system are shown in Figure 10 and Figure 11. The system consists of a digital light-processing (DLP) projector, a shutter driven by a stepper motor, a Fresnel lens, a printing platform connected to a linear stage, a resin receptacle with vertically adjustable support, and a control system (not shown in the figure).

The DLP projector gets image information from a computer and project the image upon the resin surface through a Fresnel lens. DLP (Digital Light Processing) is a technology widely used for projecting images from a monitor onto a large screen for presentation purposes. A DLP projector uses an optical semiconductor known as the DLP chip, which contains a rectangular array of up to 8 million hinge-mounted microscopic mirrors that tilt either toward the light source in a DLP projection system (ON) or away from it (OFF). This creates a light or dark pixel on the projection surface. DLP projectors have drawn attention as a light source for curing the resin in a SL system (Liska et al. 2007, Mapili et al. 2008) due to its high resolution. SL systems using DLP projectors are sometimes referred to as 3D DLP printers. In the current system, a PLD projector (Pro8300,

ViewSonic Corp., Walnut, California, USA) is mounted on top of the resin receptacle and the lens. This design minimizes the loss of illumination intensity during long distance of light travel and reflection.

A shutter made of opaque cardboard is placed under the projector to control illumination time. A stepper motor controls the position of the shutter. The stepper motor with a driver (IM483I, Schneider Electric Motion USA, Marlborough, CT, USA), is
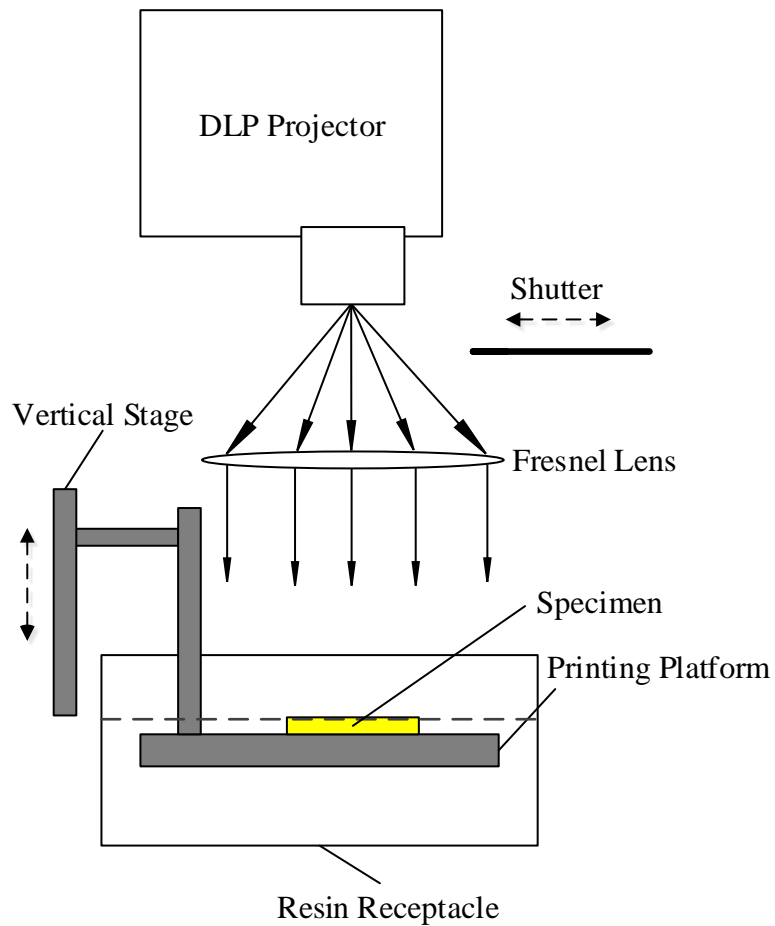
Figure 10. A schematic of the in-house developed additive manufacturing setup. The stepper motor, the control system, the support for the receptacle, and the titling stage are not included. Note that this figure is note drawn to scale.
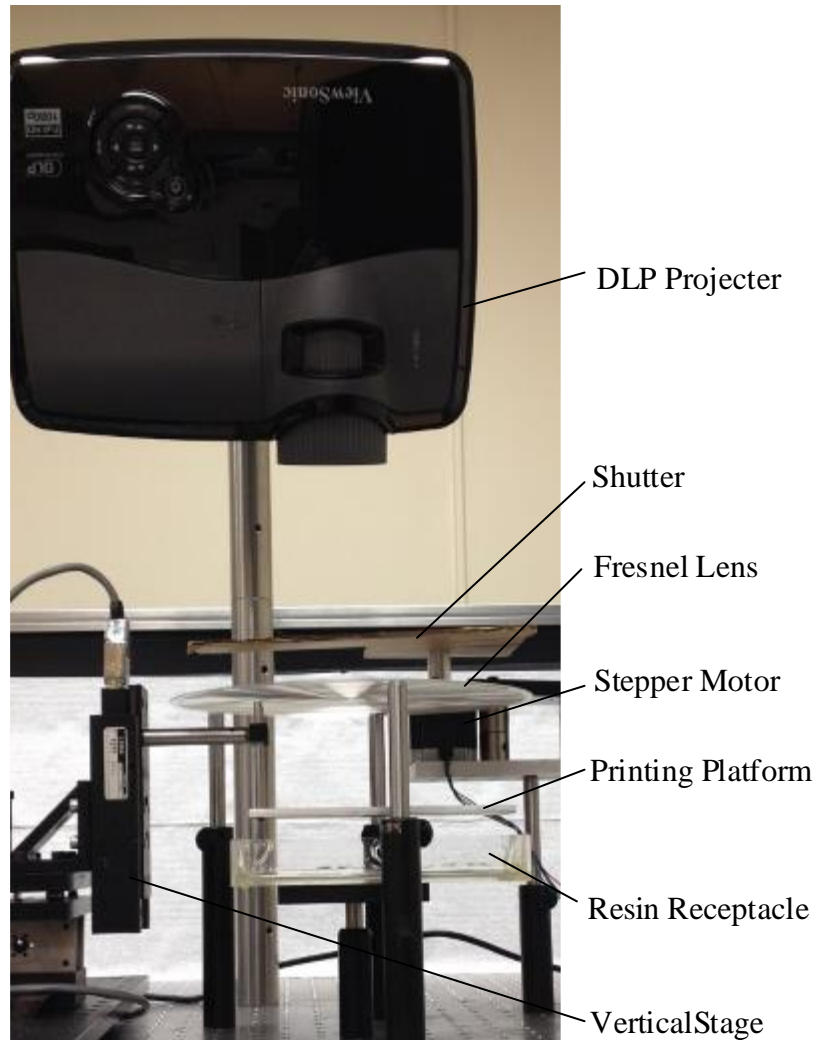
Figure 11. Photograph of the additive manufacturing system. The control system is not shown in this figure.

connected to a computer and controlled by a MATLAB program. When the shutter is open, light from the projector illuminates the resin and cure a thin layer. When the shutter is closed, the light is blocked and the printing platform moves down and up to recoat a new layer of liquid resin. With this shutter, we can flexibly control the curing time for each layer without turning the project on and off.

Below the shutter is a Fresnel lens (10.4" diameter, 9.0" focal length, Edmund Optics Inc., Barrington, NJ, USA). With careful alignment, the projector head is placed at the focal point of the Fresnel lens. When the shutter is open, divergent light from the projector is largely collimated after travelling through the Fresnel lens. The Fresnel lens, taking the form of a flat sheet, is much thinner than a conventional convex lens with the same focal length. A short focal length reduces the distance between the projector and the lens, allowing a more compact and rigid design of the illumination system. In addition, with a large functioning area, the Fresnel lens can capture more light from the light source, taking full advantage of the light intensity.

The printing platform is machined for an aluminum plate and attached to a linear stage (LS-50A, Applied Scientific Instrumentation, Eugene, OR, USA) with a submicron precision of positioning. The same MATLAB program as used to control the shutter controls the vertical movement of the platform and the stage. The linear stage is fixed on top of a tilt stage (Model 39, Newport Corp., Irvine, CA, USA) with an angle bracket. Before printing, the printing platform is leveled by adjusting the tilt stage. The height of the resin receptacle is adjustable for easy installation and removal. The control system consists of two computers, one for controlling the digital printing pattern and the other for controlling the movement of the shutter and the printing platform using a MATLAB program.

In this system, a deep-dip coating (Choi et al. 2011) process is used to deposit very thin layers of resin. Typically, a thin layer is printed by executing the following steps (assuming the shutter is initially closed):

1) Lower the printing platform into the resin for 3 mm;

2) Hold 30 seconds for stabilization;

3) Lift the platform for 2.8 mm;

4) Hold 60 seconds for stabilization;

5) Open the shutter;

6) Wait 10 seconds for the resin layer to cure;

7) Close the shutter;

8) Finish printing of the current layer and repeat steps 1-7 for printing the next layer.

For fabrication of a heterogeneous specimen, the printing process starts with merging the printing platform in a resin and building the first portion according to a printing pattern. Then, the platform is taken out of the resin, cleaned and merged into a second resin. The remaining portion of the specimen is built according to a conjugate printing pattern. Similarly, the preparation of a homogeneous specimen is done using a single resin and a single printing pattern.

4.2   TDCB Specimen Design

The tapered double-cantilever beam (TDCB) test configuration is used for fracture tests of both homogeneous and heterogeneous specimens. This specimen design was first introduced by Beres et al. (1997) and was widely used in various engineering applications (Blackman et al. 2003, Qiao et al. 2003, Brown et al. 2006, Brown 2011). A homogeneous TDCB specimen and a schematic showing the specimen dimensions are presented in Figure 12. All the specimens in this study are fabricated and machined to the
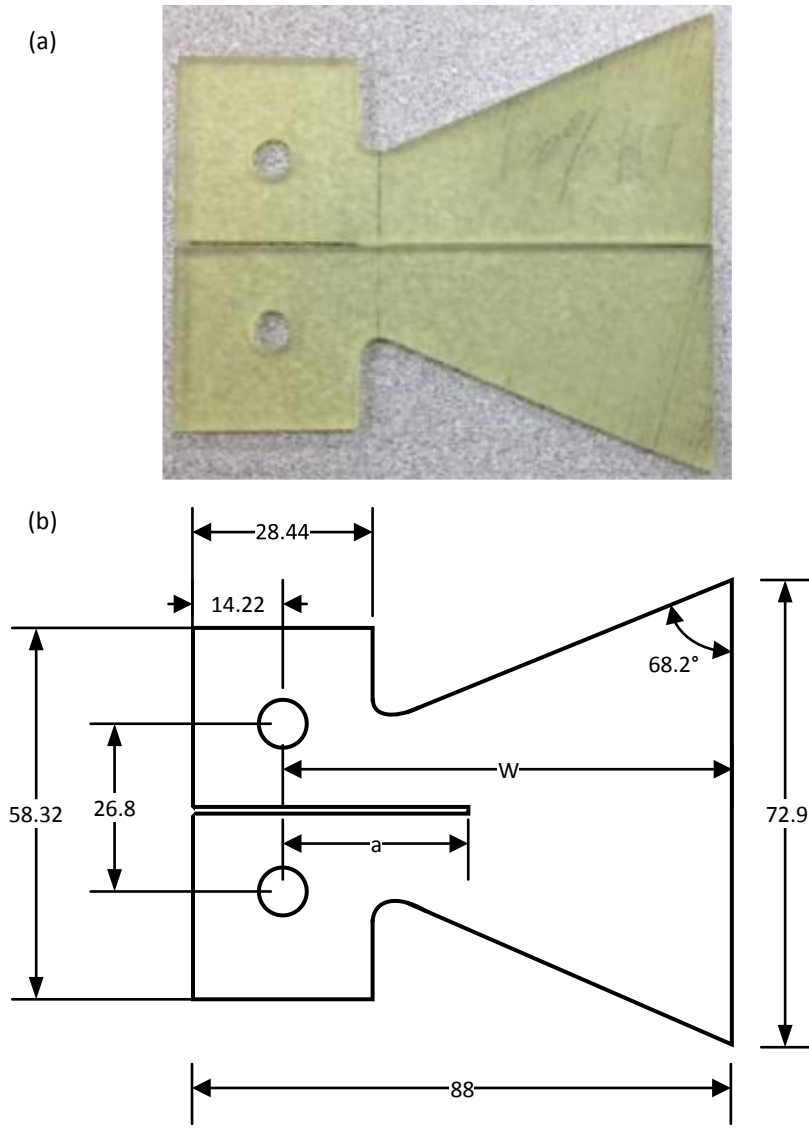
Figure 12. (a) Homogeneous TDCB specimen (100% HT), (b) A schematic drawing showing the dimensions of the TDCB specimen used in this thesis. Units: mm

same dimensions for experimental consistency. In most of the fracture tests, side V-grooves are cut into both surfaces of the specimen to prevent crack deflection. Before each monotonic fracture toughness test, cyclic fatigue loading is applied to sharpen the initial crack tip. A web camera (HD Pro C920, Logitech, Newark, CA, USA) is used to take successive snapshots during the fracture test. With a plane polariscope consisting of a fiber

optic illuminator (AmScope HL250-AY) and two linear polarizers, the crack tip position is accurately identified and recorded.

The TDCB specimen possesses a constant K_I region by continuously varying the specimen height. According to Beres et al. (1997) , when $0.2 \leq a/W \leq 0.5$, the normalized Mode I stress intensity factor ($\left(K_I B\sqrt{W}\right)/F$) is constant regardless of the crack length (a). This theory can be expressed by Equation (14):

$$\frac{K_I B\sqrt{W}}{F} = x \qquad (14)$$

where F is the load applied, and x is a constant which depends on the dimensions of the specimen and side V-grooves. For all the experiments in this thesis, B denotes the thickness of the side-grooved crack plane. In the original work, the value of x is obtained from finite element analysis.

To accommodate the additive manufacturing setup, the dimensions of the TDCB specimens fabricated in this study are slightly different from the original design in Beres et al. (1997). In addition, we use a groove angle of $60\,°$ in contrast to $45\,°$ and $90\,°$ used in the original design. With these variations, we have performed a finite element analysis to verify the existence of the constant K_I region and calibrate the value of x. In this finite element analysis, an exterior cohesive zone law for Mode I crack growth is employed. This cohesive zone law defines the cohesive zone parameters (σ_m, δ_c) from the Young's Modulus, critical energy release rate, and cohesive element size. A brief description of this exterior cohesive zone law is presented in Appendix B. The finite element analysis gives x = 13.06.

4.3   Characterization of Homogeneous Materials

In this work, two types of photo-polymerizable resins are chosen as the base materials: Spot-E and Spot-HT (Spot-A Materials, Barcelona, Spain). Both resins have high cure speed (in the near UV and visible spectrum), low viscosity and low health risk. Spot-E is formulated using base products that provide great elongation behavior of up to 100 percent. It can be used in applications needing rubbery, soft yet resilient materials. Spot-HT is used to print objects for extra hardness, toughness, impact resistance, abrasion resistance, weatherability, and chemical and water resistance. The two resins can be mixed in any ratio to print objects with material properties in-between the base materials. In the following discussions, the mixed resins are denoted by the concentration of Spot-HT resin, including 10% HT, 20% HT, 30% HT, 40% HT, and 60% HT. The two base materials are denoted as 100% E and 100% HT, respectively.

4.3.1   Elastic Modulus Measurement

The elastic moduli of the base printing materials (cured from a single or mixed resin) are necessary for designing heterogeneous materials with well-controlled elastic properties. In this work, the elastic moduli are measured by using a custom-made three-point bending setup equipped with an S-type load cell (CZL301C, Phidgets, Inc., Calgary, Alberta, Canada). The homogeneous test specimens have rectangular cross sections with dimensions of 142 mm $\times$ 31 mm. The thickness of the specimens varies within 5-7 mm. During the bending test, the full-field in-plane displacement is measured using the digital

image correlation (DIC) method (Peters and Ranson 1982, Sutton et al. 1983, Chu et al. 1985). Spray painting is used to generate a sparkle pattern on the specimen surface as required by the DIC analysis. Finally, the elastic modulus of the specimen is calculated from the beam deflection curve extracted from the displacement field and the corresponding force applied.
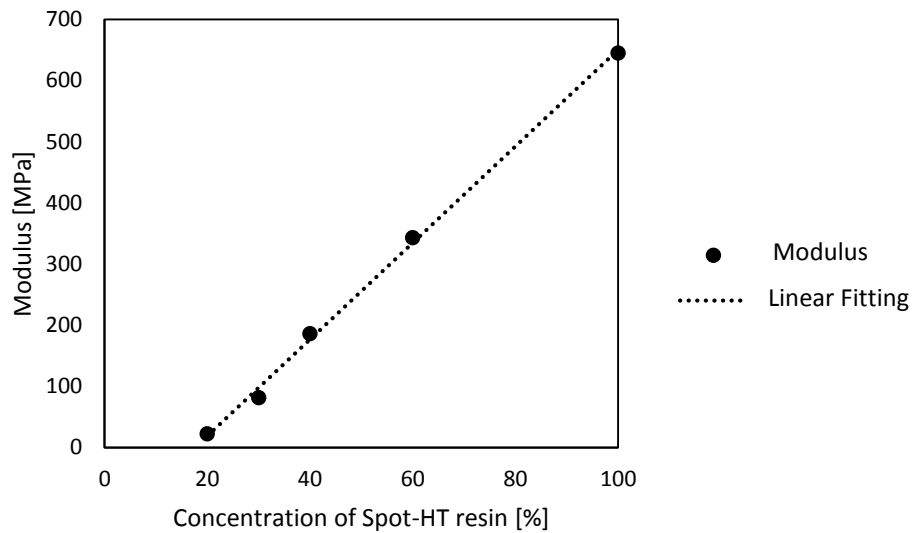
Figure 13. Relationship between the elastic modulus and the concentration of Spot-HT resin

The measured elastic moduli of different resins are shown in Figure 13. There is a very nice linear correlation between the elastic modulus and the concentration of Spot-HT, which suggests a simple linear mixture rule can be applied. The modulus measurement is not performed for low concentration of Spot-HT (less than 20%) because of the high viscosity and rubbery nature of the material in this regime.

4.3.2   Fracture Toughness Measurement

Fracture toughness is a material property that describes the ability to resist fracture. It is one of the most important criteria for material selection in engineering applications. The fracture toughness of a material is characterized by the critical stress intensity factor K_{IC}. In the current research, the K_{IC} values of the homogeneous materials are measured and compared with those of the heterogeneous materials. These intrinsic K_{IC} values are also used as input data for the finite element analysis of heterogeneous fracture, which is presented and compared with the experimental results at the end of this chapter.
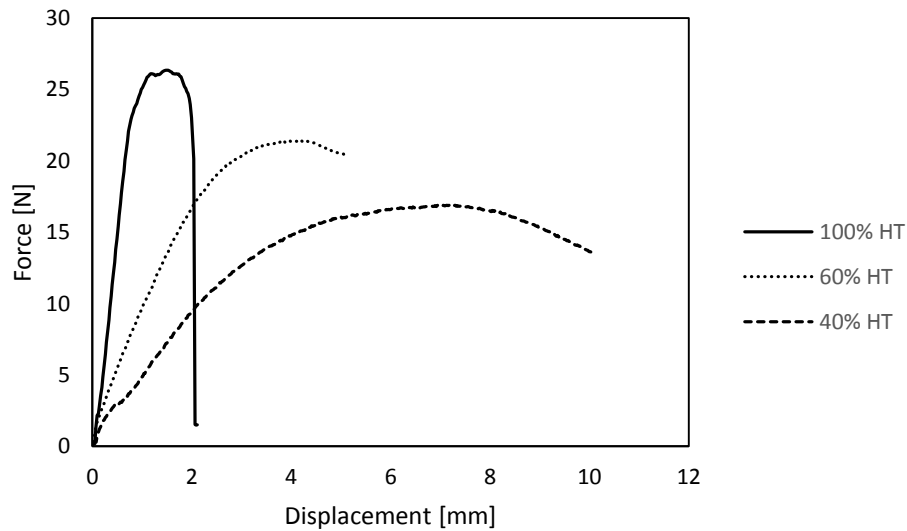
Figure 14. Load vs. displacement curves for three homogeneous TDCB specimens: 100% HT (E = 645 MPa), 60% HT (E = 343 MPa), and 40% HT (E = 186 MPa). The loading speed is kept constant at 0.003 mm/s in the three tests.

45

Table 1. Thicknesses and average loads for three homogeneous TDCB specimens.

Material	B Thickness [mm]	Average load in constant K_I region [N]	Average load per unit thickness [N/mm]
100% HT	1.84	26.16	14.22
60% HT	1.92	21.30	11.09
40% HT	2.20	16.82	7.644

Fracture tests are performed on three homogeneous specimens (100% HT, 60% HT, and 40% HT) using the TDCB test configuration. The measured load vs. displacement curves from the fracture tests are shown in Figure 14. Each of these curves exhibits a flat plateau region when the crack tip is located in the constant K_I region ($0.2 \leq a/W \leq 0.5$). The critical fracture load is calculated as the average of the plateau region, and is used for determining the critical stress intensity factor K_{IC} according to Equation (14). The critical energy release rate Γ is then calculated from the Young's modulus and K_{IC} according to

$$\Gamma = K_{IC}^2 / E .$$

The measured K_{IC} and Γ values of the three homogeneous materials are presented in Figure 15. As we can see, the K_{IC} value increases as the concentration of Spot-HT resin increases. The variation in Γ is relatively small for different concentrations of Spot-HT resin. The average Γ value of 0.774 KJ/m^2 is used for the later calculations and finite element simulations.
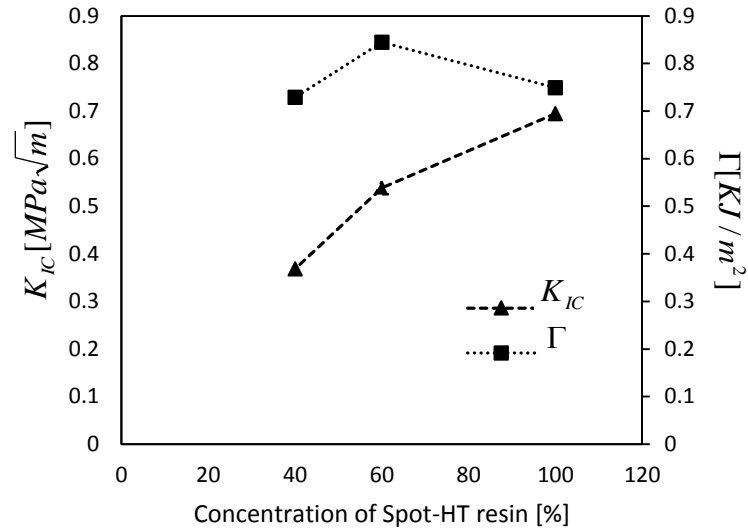
Figure 15. Critical stress intensity factors and critical energy release rates of three homogeneous materials with different concentration of Spot-HT resin.

4.3.3 Determination of Cohesive Zone Parameters

Due to plasticity or microcracking, a nonlinear zone exists ahead of the crack tip in many engineering materials (Elices et al. 2002). Various cohesive zone models have been developed to characterize this nonlinear zone. At the same time, the experimental measurement of cohesive zone laws has also attracted the interest of many researchers (Pandya and Williams 2000, Hong et al. 2009). The knowledge of cohesive zone parameters is necessary for the computational modelling of heterogeneous fracture. While an exact cohesive traction-separation law for the photo-cured polymeric materials used in this research is unclear, we employ a bilinear cohesive zone model to describe the fracture process zone as an approximation. The cohesive zone parameters are then experimentally

determined within this framework. The detailed description of the bilinear cohesive zone law is presented earlier in Section 3.2.
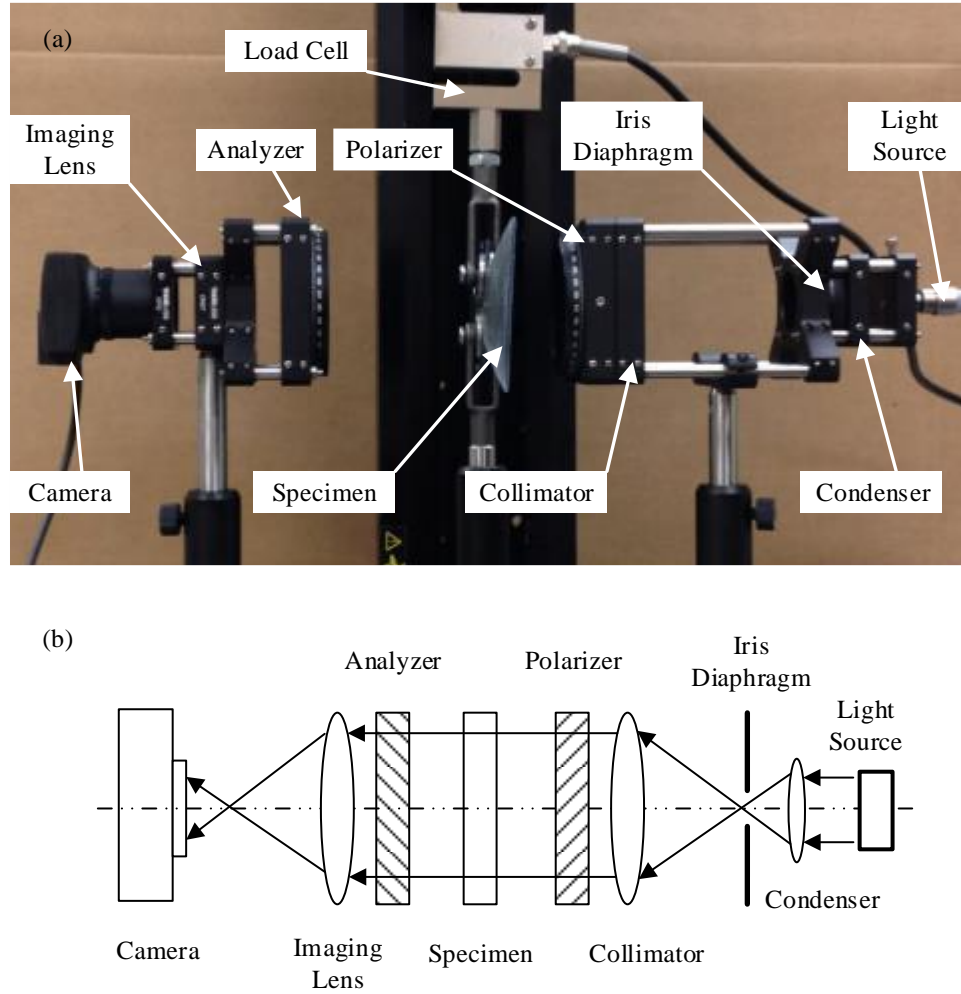
Figure 16. (a) A photograph and (b) a schematic of a plane polariscope setup.

With the critical energy release rate obtained from previous experiments, there is only one cohesive zone parameter to be determined in the cohesive zone model — the maximum normal traction σ_m. An iterative comparison process between the fracture tests and finite simulations is employed to determine this parameter for two homogeneous

materials (60% HT and 100% HT). First, the cohesive zone length of a homogeneous material is measured experimentally through the fracture test of a TDCB specimen. Then, finite element simulations of crack propagation in a homogeneous medium are performed using different σ_m values. The true value of maximum normal traction σ_m is determined by matching the simulated cohesive zone length with the experimental measurement with a binary search. The σ_m values are identified as 20.4 MPa for the 60% HT resin and 13.0 MPa for the 100% HT resin, respectively.

In this work, a plane polariscope is used to accurately measure the cohesive zone length during the fracture test of a homogenous TDCB specimen, as shown in Figure 16. Side V-grooves are not cut in this specimen to ensure a reliable identification of the cohesive zone. Based on photoelasticity, a plane polariscope is able to visualize stress fields through stress (or strain) induced birefringence. The plane polariscope includes a pair of polarizers, a white light source (Dyonics 300XL, Smith & Nephew, Inc., Andover, MA, USA), and a digital camera (DCC1545M, Thorlabs Inc., Newton, NJ, USA). The two polarizers, namely the polarizer and the analyzer, have crossed polarization axes on different sides of the specimen. The light intensity recorded by the camera is given by the following equation (Asundi 1998):

$$I = A^2 \left(\sin^2 2\theta \right) \sin^2 \frac{\alpha}{2} \tag{15}$$

where A is the amplitude of the input light vector, θ is the angle between the polarizer axis and the principle stress direction in the specimen, and α is the relative phase retardation. α is further related to the principal stress difference through:

$$\alpha = \frac{2\pi d C(\sigma_1 - \sigma_2)}{\lambda} \tag{16}$$

where λ is the wavelength of light, C is the stress-optic coefficient, σ_1 and σ_2 are the principal stresses, and d is the specimen thickness.
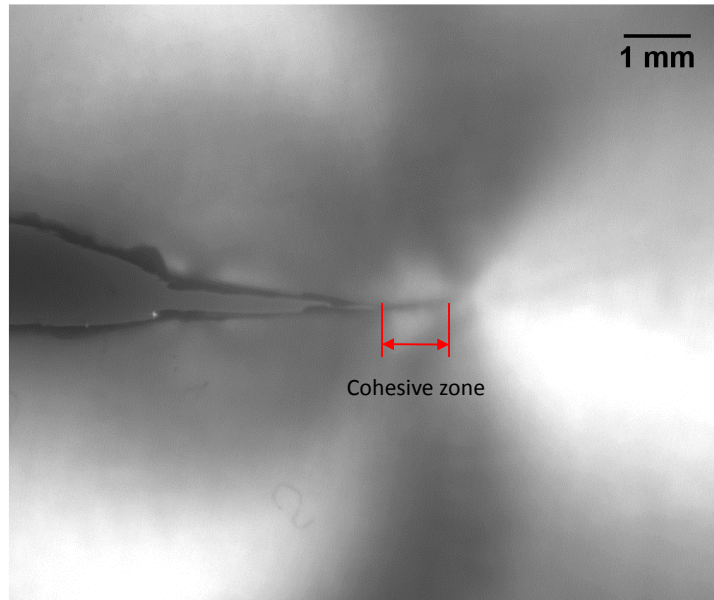
Figure 17. Birefringence image of a 60% HT TDCB specimen during fracture test

In the current experiments, the polarizer axis is fixed at 45° relative to the horizontal axis. According to the analytical stress fields of a Mode I crack tip in a linear elastic, isotropic material (Anderson 2005), σ_1 and σ_2 are close ahead of the crack tip, which results in a low light intensity in this region. However, σ_2 is dominant in the cohesive zone. Thus, the area near the cohesive zone stands out as a bright region. The test result of 60% HT is shown in Figure 17. The cohesive zone lengths of 60% HT and 100% HT resins are determined as 1.13 mm and 0.85 mm, respectively.

4.4　Fracture Tests of Heterogeneous Materials

Fracture tests of heterogeneous materials are also performed using the TDCB test configuration. As discussed in Section 4.2, the TDCB specimen design creates a constant K_I region by varying the specimen height, which helps to stabilize crack propagation in the heterogeneous material systems.
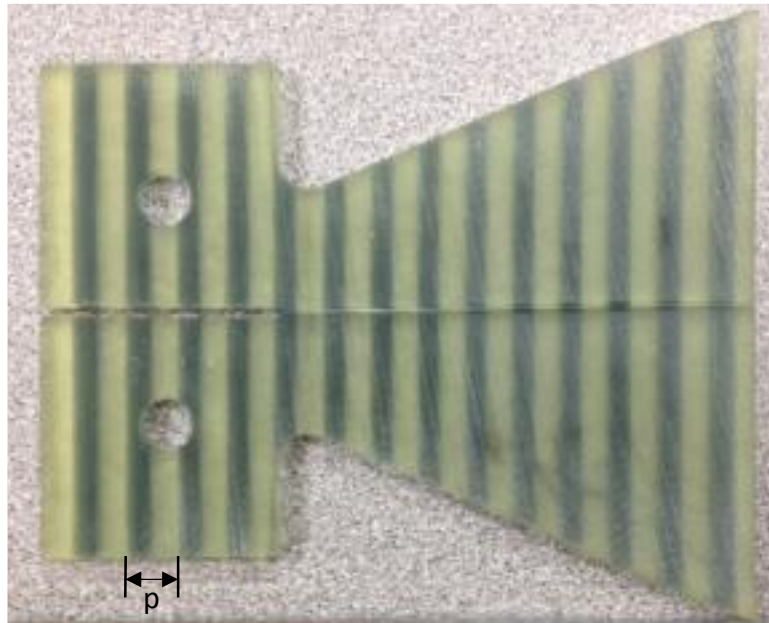
Figure 18. Photograph of a heterogeneous TDCB specimen consisting of alternating stiff stripes (100% HT, light color, $E_S = 645$ MPa) and compliant stripes (60% HT, dark color, $E_C = 343$ MPa). Other parameters are: period $p = 6$ mm, stiff phase volume fraction $\lambda = 0.53$, thickness of the crack plane $B = 1.88$ mm.

In this thesis, we investigated the fracture behavior of a heterogeneous TDCB specimen with optimized material and geometrical design, as shown in Figure 18. The heterogeneous TDCB specimen is a model material system that mimics the key microstructural features of many tough biological materials, such as bones, seashells, and teeth. The dimensions of this specimen are identical to those of the homogeneous TDCB specimens except for slight thicknesses difference. The heterogeneous specimen is fabricated using two different resins: 100% HT ($E_S = 645$ MPa) and 60% HT ($E_C = 343$ MPa), leading to a modulus mismatch ratio of $E_S / E_C = 1.88$. The spatial period of heterogeneity (p) is 6 mm, and the stiff phase has a volume fraction (λ) of 0.53.

Figure 19 shows the load-displacement curve from the fracture test of the heterogeneous TDCB specimen. Figure 20 includes a few snapshots of the specimen during crack propagation. The snapshots, which correspond to the six data points in Figure 19, record the crack extension within one period of spatial heterogeneity. The stress intensity factors for the six data points are calculated based on Equation (14) and
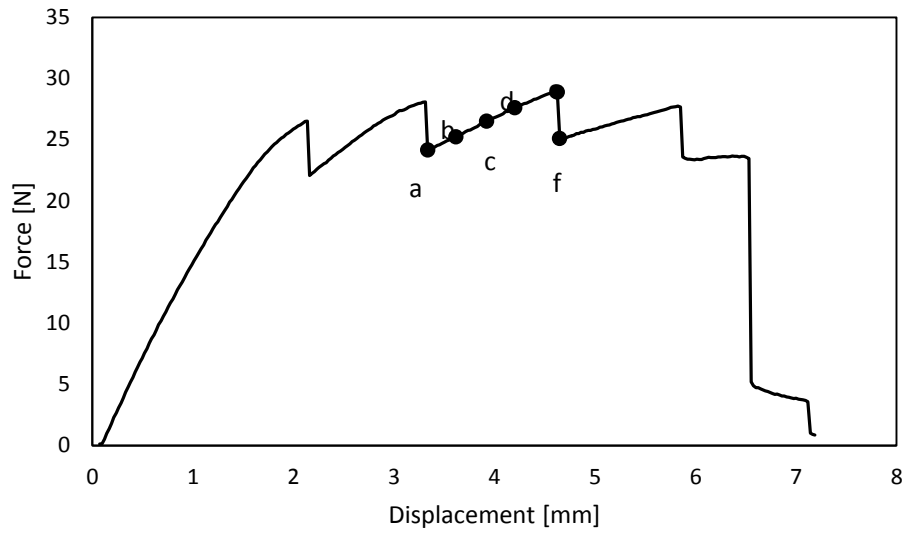
Figure 19. Load vs. displacement curve for a heterogeneous TDCB specimen. The loading speed is 0.003 mm/s.
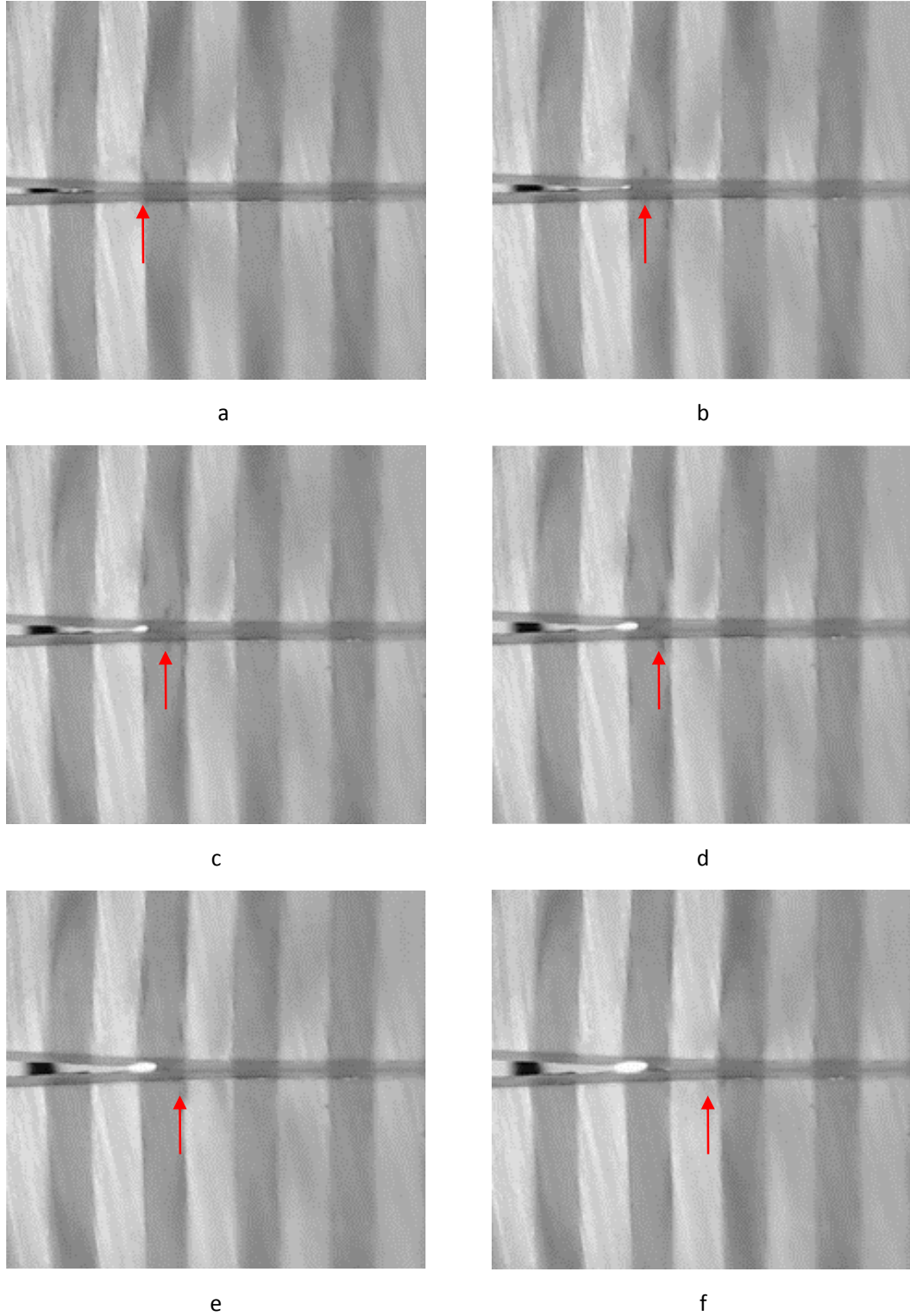
Figure 20. Snapshots of crack growth in the heterogeneous TDCB specimen. The snapshots correspond to the six data points labeled in Figure 19. The arrows indicate the crack tip positions.
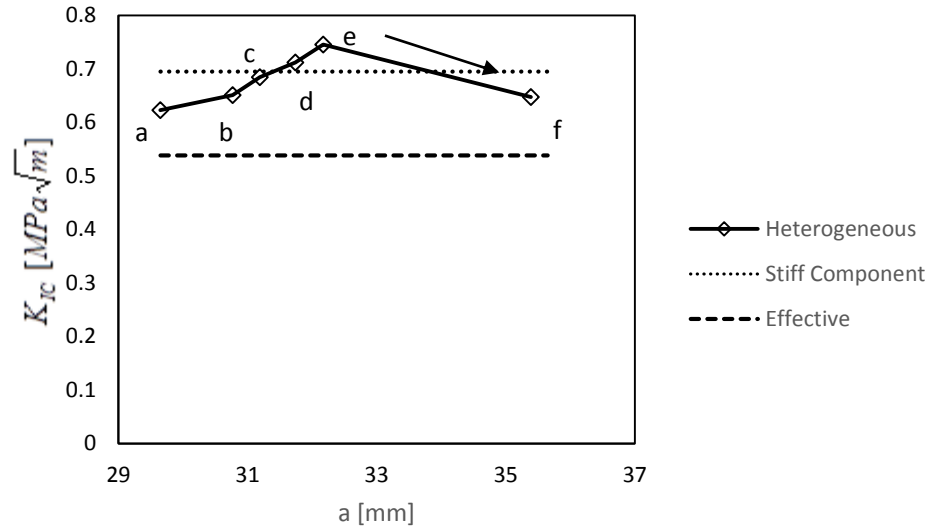
Figure 21. Fracture resistance curve for the heterogeneous TDCB specimen. The arrows from e to f indicates unstable crack propagation. The Mode I stress critical intensity factors of the homogeneous stiff (100% HT) and compliant (60% HT) materials are presented for comparison.

the x value from Section 4.2. With the crack lengths measured from the snapshots, a fracture resistance curve for the heterogeneous specimen is constructed as seen in Figure 21. The fracture toughness of the stiff component and the effective fracture toughness calculated from S_{ij} are also included in Figure 21.

In Figure 19, the load increases linearly as the displacement increases during the initial loading period. When the crack starts to propagate, the slope of the curve will drop. During crack propagation, the load varies periodically due to the material heterogeneity in the specimen. From the crack tip positions seen in Figure 20, it is obvious that the crack experiences relatively stable propagation within the compliant region and the load keeps increasing as the crack extends. After passing the compliant-to-stiff interface, the crack snaps through the entire stiff stripe and reaches the next stiff-to-compliant interface. The load drops suddenly (from point 'e' to 'f') during the snap-through process. This kind of

unstable crack propagation is inherent in heterogonous materials. With the TDCB specimen design, we are able to control the instability by creating the constant K_I region, which prevents the catastrophic failure when the crack is penetrating the interface. From Figure 20, we can also see that the crack path is straight and there is no deflection or interfacial delamination. This is due to the grooves that predefine the crack path and the strong interfacial bonding between two material constituents.

It can be seen from Figure 21, the heterogeneous specimen exhibits higher fracture toughness when compared with its stiff constituent or the effective fracture toughness. Within the compliant region, the stress intensity factor keeps increasing as the crack extends. In the stiff region, the stress intensity factor drops dramatically as the crack snaps through. Qualitatively, the experimental results are in good agreement with the simulation results presented in Chapter 3.

4.5   Comparison between Experiments and Simulations

To quantitatively compare the experimental and simulation results, the material properties of the two constituents obtained from the previous experiments are input into the finite element model to simulate the crack propagation in the heterogeneous material system. The input material parameters include the Young's moduli, critical energy release rates, and cohesive zone parameters of the two homogenous constituent materials (60% HT and 100% HT). The T-stress value in the heterogeneous test specimen is also calculated and input into the finite element model. A detailed calculation of T-stress is presented in Appendix C.

Figure 22 illustrates the normalized fracture resistance curves from the experimental measurement and the finite element simulation. The general trends of the two curves are very similar. In both curves, the stress intensity factor increases as the crack extends in the compliant region and drops as the crack extends into the stiff region. Due to the implementation of the instability control algorithm, the crack propagation in the stiff region is stabilized in the finite element model, resulting in a complete determination of the fracture resistance curve. In contrast, the crack growth in the stiff region is unstable in the displacement-controlled experiment. It is noted that a secondary crack is formed during crack arrest in the simulation but not in the experiment. This discrepancy is possibly due to the low spatial resolution of the imaging system, which limits the ability to visualize the secondary crack in the experiment.
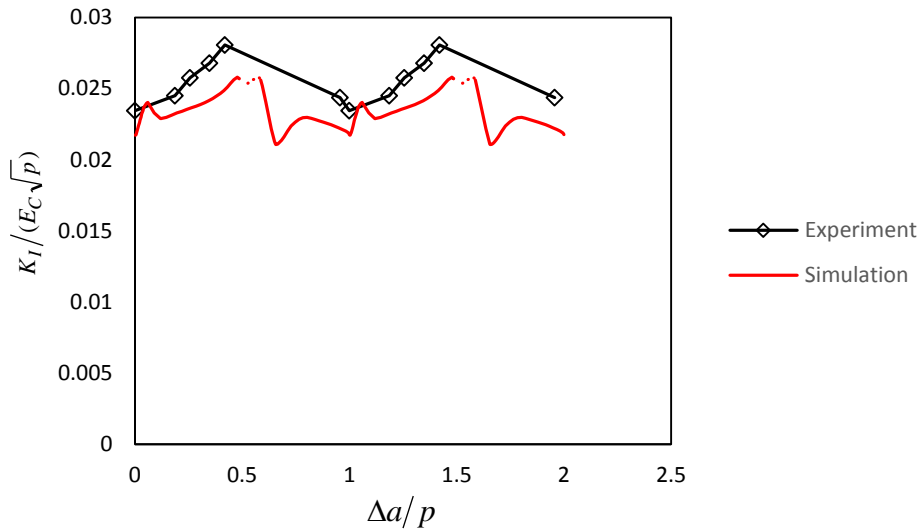
Figure 22. The normalized fracture resistance curves from the experimental measurement and the finite element simulation. Note that the doted red line represents the secondary crack recorded from the simulation.

As we can see from Figure 22, the stress intensity factor from the simulation is somewhat smaller than that from the experiment. This difference may be attributed to the plasticity and viscoelasticity of the real material system which are not included in the finite element simulation.

4.6   Conclusions

The experimental investigation of heterogeneous fracture is presented in this chapter. First, an additive manufacturing setup is developed based on stereolithography. This setup is used to build test specimens with well-controlled structural and material properties. Then, homogeneous specimens are tested to characterize the mechanical properties of the individual phases in the heterogeneous materials, including elastic moduli, fracture toughness, and cohesive zone parameters. Afterwards, fracture tests of heterogeneous TDCB specimens are performed to study the fracture behaviors of the heterogeneous materials. Unstable crack propagation and crack arrest at compliant-to-stiff interfaces are observed during the fracture tests. With appropriate material and geometrical parameters, the heterogeneous material system exhibits higher fracture toughness than the constituent homogenous materials. The enhancement and crack instability are explained by the elastic modulus mismatch within the heterogeneous material.. Finally, computational modelling of the crack propagation in the heterogeneous material system is performed using the material parameters obtained from the experiments. The comparison between the experimental and simulation results is presented. The experimental scheme developed in this chapter would be of great value to the fabrication and testing of heterogeneous materials with exceptional mechanical properties.

CHAPTER 5

CONCLUDING REMARKS AND FUTURE CHALLENGES

5.1   Concluding Remarks

In this thesis, an integrated computational and experimental effort is taken to study fracture in heterogeneous elastic solids. It is concluded that the elastic contrast plays an important role in determining the fracture behaviors of a heterogeneous material system. With well-controlled material and geometrical parameters, heterogeneous materials exhibit substantial enhancement in fracture toughness compared with their homogeneous constituents. Using a crack-tip-opening controlled algorithm, finite element simulations are performed to study the fracture process in a two-phase laminate composite. Computational parametric studies suggest that that large fracture toughness enhancement can be achieved with high modulus mismatch ratio, optimal stiff phase volume fraction, small cohesive zone size, and negative T-stress. Fracture tests are performed using the TDCB specimen design. With optimized material and geometrical design, heterogeneous specimens achieve higher fracture toughness than their homogenous constituents. In addition, crack instability and arrest at compliant-to-stiff interfaces are observed in the fracture tests, which is in good agreement with the computational predictions.

The combined computational and experimental study in this thesis provides a fundamental mechanistic understanding of the fracture mechanisms in brittle heterogeneous materials. The computational schemes developed and implemented here are useful tools for microstructural optimization of tough heterogeneous materials. The

experimental setups and methods used in this work offer a potential route for fabrication and testing of extreme materials with patterned heterogeneities.

5.2   Recommendations for Future Work

The present work investigates the fracture behaviors of heterogeneous materials with well-controlled material and structure properties. The TDCB specimen design used in this work can solve the instability problem effectively. However, the large T-stress associated with this design has limited its application in a broader parameter space. Future work may consider other specimen designs that are able to overcome both the instability and the T-stress problems. The material systems under current investigation exhibit structural heterogeneities on one length scale. Future work may consider heterogeneous materials with hierarchical microstructures spanning multiple length scales, which mimic the tough biological composites more closely. The investigation would require modification of the finite element model, and also more delicate fabrication and testing setups for experimentation.

THE COMPLIANCE MATRIX FOR COMPOSITE LAMINATE

In Section 3.2, a compliance matrix S_{ij} is used to characterize the effective mechanical properties in the homogenized anisotropic zone. This matrix is used for calculation of other parameters in the Abaqus user subroutine. In addition, some elements of this matrix are directly input into Abaqus as the engineering constants for the anisotropic material. Calculation of this compliance matrix is based on mechanical properties of the two constituents in the laminate structure. This appendix describes the calculation process based on the work of Liu (2005).
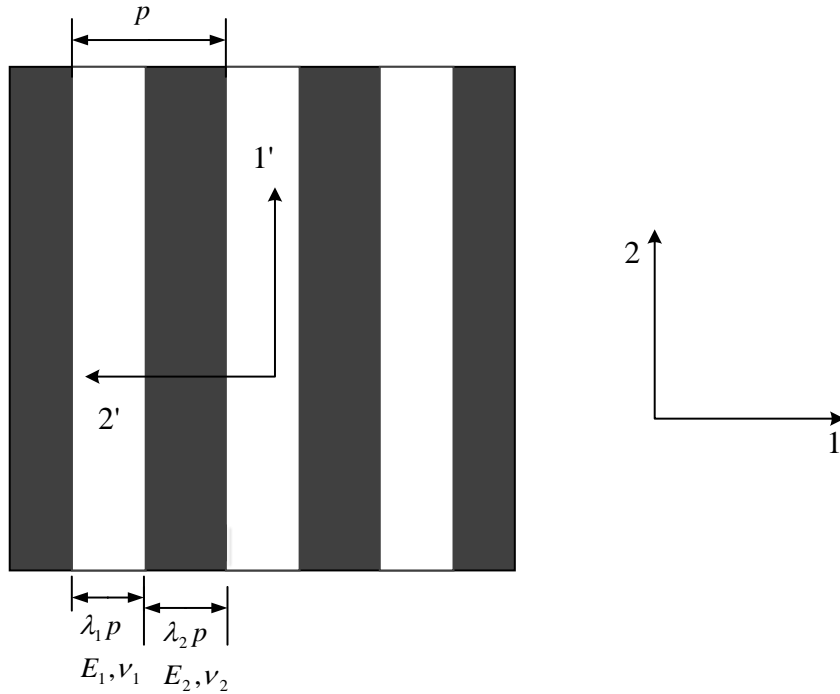
Figure 23. E_1, ν_1, E_2, ν_2 are material properties of the two constituents. p is the period of spatial heterogeneity, λ_1 and λ_2 represent the volume fraction of the two materials. Coordinate systems: 1', 2', principal material coordinates; 1, 2, laminate coordinates (global coordinates)

For uniaxial longitudinal loading, a normal load is applied in the 2-direction, which is parallel to the material orientation. Material properties can be obtained by the "rule of mixtures":

$$E_{22} = \lambda_1 E_1 + \lambda_2 E_2 \tag{17}$$

$$v_{21} = \lambda_1 v_1 + \lambda_2 v_2 \tag{18}$$

where E_{22} is the longitudinal Young's modulus and v_{21} is the longitudinal Poisson's ratio.

For uniaxial transverse loading, a normal load is applied in the 1-direction, which is perpendicular to the material orientation. In this case, the following equalities are established:

$$\frac{1}{E_{11}} = \frac{\lambda_1}{E_1} + \frac{\lambda_2}{E_2} \tag{19}$$

$$\frac{v_{12}}{E_{11}} = \frac{\lambda_{21}}{E_{22}} \tag{20}$$

where E_{11} is the transverse Young's modulus and v_{12} is the transverse Poisson's ratio. Solving for the two material constants, the following equation is obtained:

$$E_{11} = 1 \left/ \left(\frac{\lambda_1}{E_1} + \frac{\lambda_2}{E_2} \right) \right. \tag{21}$$

$$v_{12} = \frac{E_{11}}{E_{22}} \left(\lambda_1 v_1 + \lambda_2 v_2 \right) \tag{22}$$

For longitudinal shear loading (in-plane), a shear stress is applied in the 1-2 plane. Similar to the calculation for transverse Young's modulus, we have:

$$G_{21} = 1 \bigg/ \left(\frac{\lambda_1}{G_1} + \frac{\lambda_2}{G_2} \right) \tag{23}$$

where G_{21} is the longitudinal shear modulus; G_1, G_2 are the shear moduli of the two materials, calculated by the following equations:

$$G_1 = \frac{E_1}{2(1+v_1)} \tag{24}$$

$$G_2 = \frac{E_2}{2(1+v_2)} \tag{25}$$

For out of plane shear loading (2-3 plane), the following equations are established:

$$G_{32} = \lambda_1 G_1 + \lambda_2 G_2 \tag{26}$$

$$v_{32} = v_2 \tag{27}$$

Stress-strain relationship for the composite laminate can be expressed in matrix form as:

$$\left[\varepsilon_{ij} \right] = \left[S_{ij} \right] \left[\sigma_{ij} \right] \tag{28}$$

$$
\begin{bmatrix} \varepsilon_{11} \\ \varepsilon_{22} \\ \varepsilon_{33} \\ \varepsilon_{23} \\ \varepsilon_{13} \\ \varepsilon_{12} \end{bmatrix}
=
\begin{bmatrix}
1/E_{11} & -v_{21}/E_{22} & -v_{31}/E_{33} & 0 & 0 & 0 \\
-v_{12}/E_{11} & 1/E_{22} & -v_{32}/E_{33} & 0 & 0 & 0 \\
-v_{13}/E_{11} & -v_{23}/E_{22} & 1/E_{33} & 0 & 0 & 0 \\
0 & 0 & 0 & 1/G_{23} & 0 & 0 \\
0 & 0 & 0 & 0 & 1/G_{13} & 0 \\
0 & 0 & 0 & 0 & 0 & 1/G_{12}
\end{bmatrix}
\begin{bmatrix} \sigma_{xx} \\ \sigma_{yy} \\ \sigma_{zz} \\ \sigma_{yz} \\ \sigma_{xz} \\ \sigma_{xy} \end{bmatrix}
\tag{29}
$$

For a plane stress problem, the 3-direction (out-of-plane) is equivalent to the 2-direction. In addition, for shear material properties, two indices are interchangeable. As presented in Equation (3), the final expression for the compliance matrix S_{ij} is:

$$
S_{ij} = \begin{bmatrix}
1/E_{11} & -v_{21}/E_{22} & -v_{31}/E_{22} & 0 & 0 & 0 \\
-v_{12}/E_{11} & 1/E_{22} & -v_{32}/E_{22} & 0 & 0 & 0 \\
-v_{13}/E_{11} & -v_{23}/E_{22} & 1/E_{22} & 0 & 0 & 0 \\
0 & 0 & 0 & 1/G_{23} & 0 & 0 \\
0 & 0 & 0 & 0 & 1/G_{13} & 0 \\
0 & 0 & 0 & 0 & 0 & 1/G_{12}
\end{bmatrix}
$$

The calculation presented here is valid when the material coordinates and laminate coordinates are perpendicular (90 ° rotation).

APPENDIX B

AN EXTERIOR COHESIVE ZONE MODEL

In Section 4.3.2, an exterior cohesive zone model is implemented to model crack growth. Based on the previous work of Xia et al. (2009), the expressions for the cohesive zone parameters σ_m and δ_C are as follows:

$$\sigma_m = 2\sqrt{\frac{\mu\Gamma}{\pi(1-\nu)L}} \tag{30}$$

$$\delta_C = \sqrt{\frac{\pi(1-\nu)L\Gamma}{\mu}} \tag{31}$$

where μ is the shear modulus, Γ is fracture energy, L is the element size around crack tip in the finite element model.

APPENDIX C

T-STRESS IN TDCB SPECIMENS

In Section 4.5, the T-stress are obtained from the experiments and put into the finite element model. This appendix describes the calculation of T-stress during the fracture test of a TDCB specimen. Figure 24 illustrates the dimensions of a half TDCB specimen.
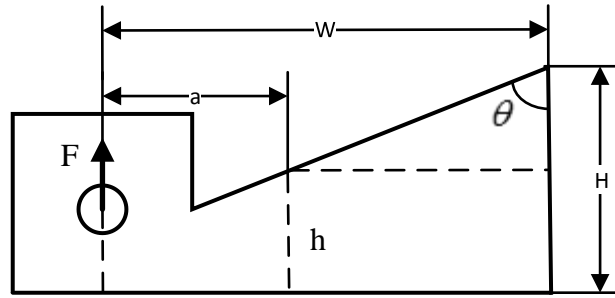
Figure 24. Calculation for T-stress in TDCB specimens

Based on Figure 12, the corresponding dimensions are: H = 36.45 mm, W = 72.78 mm, θ = 68.2°. Date point e (the peak value of load) in Figure 19 is taken as an example for T-stress calculation. At this point, F = 28.89 N, a = 32.17 mm. The thickness of the specimen in the ungrooved region is B_0 = 3.62 mm. The following equations are used to calculate the T-stress (T_{max}) near the crack tip.

$$T_{max} = \frac{Fa}{I} h \tag{32}$$

$$I = \frac{1}{12} B_0 h^3 \tag{33}$$

$$\tan\theta = \frac{W-a}{H-h} \tag{34}$$

The T-stress value is calculated with Equations (32)-(34) to be:

$$T_{max} = 7.5504\,MPa \tag{35}$$

REFERENCES

1. Anderson, T. L. (2005). <u>Fracture mechanics: fundamentals and applications</u>, CRC press.

2. Arcaute, K., et al. (2010). "Stereolithography of spatially controlled multi-material bioactive poly (ethylene glycol) scaffolds." <u>Acta biomaterialia</u> **6**(3): 1047-1054.

3. Arcaute, K., et al. (2006). "Stereolithography of three-dimensional bioactive poly (ethylene glycol) constructs with encapsulated cells." <u>Annals of biomedical engineering</u> **34**(9): 1429-1441.

4. Asundi, A. K. (1998). <u>Recent advances in photoelastic applications</u>. International Conference on Fiber Optics and Photonics: Selected Papers from Photonics India'96, International Society for Optics and Photonics.

5. Banerjee, R., et al. (2004). "Comparison of microstructural evolution in laser-deposited and arc-melted In-Situ Ti-TiB composites." <u>Metallurgical and Materials Transactions A</u> **35**(7): 2143-2152.

6. Banks-Sills, L., et al. (2005). "Methods for calculating stress intensity factors in anisotropic materials: Part I—< i> z</i>= 0 is a symmetric plane." <u>Engineering fracture mechanics</u> **72**(15): 2328-2358.

7. Bechtle, S., et al. (2010). "Crack arrest within teeth at the dentinoenamel junction caused by elastic modulus mismatch." <u>Biomaterials</u> **31**(14): 4238-4247.

8. Beres, W., et al. (1997). "A tapered double-cantilever-beam specimen designed for constant-K testing at elevated temperatures." <u>Journal of testing and evaluation</u> **25**: 536-542.

9. Biner, S. and S. Y. Hu (2009). "Simulation of damage evolution in composites: A phase-field model." <u>Acta Materialia</u> **57**(7): 2088-2097.

10. Blackman, B., et al. (2003). "The calculation of adhesive fracture energies in mode I: revisiting the tapered double cantilever beam (TDCB) test." <u>Engineering fracture mechanics</u> **70**(2): 233-248.

11. Blanks, K., et al. (1998). "Crack deflection in ceramic laminates using porous interlayers." <u>Journal of the European Ceramic Society</u> **18**(13): 1945-1951.

12. Bletzinger, K.-U. and E. Ramm (2001). "Structural optimization and form finding of light weight structures." <u>Computers & Structures</u> **79**(22): 2053-2062.

13. Bocca, P. and A. Carpinteri (1990). "Snap-back fracture instability in rock specimens: experimental detection through a negative impulse." Engineering Fracture Mechanics **35**(1): 241-250.

14. Bosco, C., et al. (1990). "Fracture of reinforced concrete: scale effects and snap-back instability." Engineering Fracture Mechanics **35**(4): 665-677.

15. Bower, A. F. and M. Ortiz (1991). "A three-dimensional analysis of crack trapping and bridging by tough particles." Journal of the Mechanics and Physics of Solids **39**(6): 815-858.

16. Brown, E. (2011). "Use of the tapered double-cantilever beam geometry for fracture toughness measurements and its application to the quantification of self-healing." The Journal of Strain Analysis for Engineering Design **46**(3): 167-186.

17. Brown, E., et al. (2006). "Fatigue crack propagation in microcapsule-toughened epoxy." Journal of materials science **41**(19): 6266-6273.

18. Bueckner, H. F. (1987). "Weight functions and fundamental fields for the penny-shaped and the half-plane crack in three-space." International Journal of Solids and Structures **23**(1): 57-93.

19. Chan, V., et al. (2012). "Multi-material bio-fabrication of hydrogel cantilevers and actuators with stereolithography." Lab on a Chip **12**(1): 88-98.

20. Choi, J.-W., et al. (2011). "Multi-material stereolithography." Journal of Materials Processing Technology **211**(3): 318-328.

21. Choi, J.-W., et al. (2010). "Multi-material microstereolithography." The International Journal of Advanced Manufacturing Technology **49**(5-8): 543-551.

22. Chu, T., et al. (1985). "Applications of digital-image-correlation techniques to experimental mechanics." Experimental mechanics **25**(3): 232-244.

23. Claussen, N. (1976). "Fracture Toughness of Al2O3 with an Unstabilized ZrO2Dispersed Phase." Journal of the American Ceramic society **59**(1‐2): 49-51.

24. Clegg, W. J., et al. (1990). "A simple way to make tough ceramics." Nature **347**(6292): 455-457.

25. Elices, M., et al. (2002). "The cohesive zone model: advantages, limitations and challenges." Engineering fracture mechanics **69**(2): 137-163.

26. Evans, A. and K. Faber (1981). "Toughening of ceramics by circumferential microcracking." Journal of the American Ceramic Society **64**(7): 394-398.

27. Farnworth, W. M. (2003). Stereolithographic method for applying materials to electronic component substrates and resulting structures, Google Patents.

28. Fratzl, P., et al. (2007). "Hindered crack propagation in materials with periodically varying Young's modulus—lessons from biological materials." Advanced Materials **19**(18): 2657-2661.

29. Fratzl, P. and R. Weinkamer (2007). "Nature's hierarchical materials." Progress in Materials Science **52**(8): 1263-1334.

30. Gao, H. (1991). "Fracture analysis of nonhomogeneous materials via a moduli-perturbation approach." International Journal of Solids and Structures **27**(13): 1663-1682.

31. Gao, H., et al. (2003). "Materials become insensitive to flaws at nanoscale: lessons from nature." Proceedings of the national Academy of Sciences **100**(10): 5597-5600.

32. Gao, Y. and A. Bower (2004). "A simple technique for avoiding convergence problems in finite element simulations of crack nucleation and growth on cohesive interfaces." Modelling and Simulation in Materials Science and Engineering **12**(3): 453.

33. Gibson, I., et al. (2002). "Rapid prototyping for architectural models." Rapid prototyping journal **8**(2): 91-95.

34. Gonzalez, J. and J. Lambros (2013). "Crack path selection in microstructurally tailored inhomogeneous polymers." Experimental Mechanics: 1-16.

35. Greer, C., et al. (1996). "Processing of carbon fiber reinforced composites by three dimensional photolithography." Proc. SFF, Texas: 307-311.

36. Griffith, M. L. and J. W. Halloran (1996). "Freeform fabrication of ceramics via stereolithography." Journal of the American Ceramic Society **79**(10): 2601-2608.

37. Hannink, R. and M. Swain (1994). "Progress in transformation toughening of ceramics." Annual Review of Materials Science **24**(1): 359-408.

38. Hong, S., et al. (2009). "Cohesive-zone laws for void growth—I. Experimental field projection of crack-tip crazing in glassy polymers." Journal of the Mechanics and Physics of Solids **57**(8): 1357-1373.

39. Hull, C. W. (1986). Apparatus for production of three-dimensional objects by stereolithography, Google Patents.

40. Hutchinson, J. W. (1989). "Mechanisms of toughening in ceramics." Theoretical and applied mechanics: 139-144.

41. Ighodaro, O. L. and O. I. Okoli (2008). "Fracture toughness enhancement for alumina systems: A Review." International Journal of Applied Ceramic Technology **5**(3): 313-323.

42. Jackson, B., et al. (2000). Discrete multi-material selective laser sintering: development for an application in complex sand casting core arrays. Proceedings of Solid Freeform Fabrication Symposium, The University of Texas.

43. Jafari, M., et al. (2000). "A novel system for fused deposition of advanced multiple ceramics." Rapid Prototyping Journal **6**(3): 161-175.

44. Khalil, S., et al. (2005). "Multi-nozzle deposition for construction of 3D biopolymer tissue scaffolds." Rapid Prototyping Journal **11**(1): 9-17.

45. Kleebe, H. J., et al. (1999). "Microstructure and fracture toughness of Si3N4 ceramics: combined roles of grain morphology and secondary phase chemistry." Journal of the American Ceramic Society **82**(7): 1857-1867.

46. Koester, K. J., et al. (2008). "The true toughness of human cortical bone measured with realistically short cracks." Nature Materials **7**(8): 672-677.

47. Kruth, J.-P. (1991). "Material incress manufacturing by rapid prototyping techniques." CIRP Annals-Manufacturing Technology **40**(2): 603-614.

48. Kruth, J.-P., et al. (1998). "Progress in additive manufacturing and rapid prototyping." CIRP Annals-Manufacturing Technology **47**(2): 525-540.

49. Kumar, S. and J.-P. Kruth (2010). "Composites by rapid prototyping technology." Materials & Design **31**(2): 850-856.

50. Leguillon, D. (2002). "Strength or toughness? A criterion for crack onset at a notch." European Journal of Mechanics-A/Solids **21**(1): 61-72.

51. Leguillon, D. and E. Martin (2013). "The strengthening effect caused by an elastic contrast—part I: the bimaterial case." International Journal of Fracture **179**(1-2): 157-167.

52. Leguillon, D. and E. Martin (2013). "The strengthening effect caused by an elastic contrast—part II: stratification by a thin stiff layer." International Journal of Fracture **179**(1-2): 169-178.

53. Leguillon, D., et al. (2006). "Prediction of crack deflection in porous/dense ceramic laminates." Journal of the European Ceramic Society **26**(3): 343-349.

54. Li, Y. and M. Zhou (2013). "Prediction of fracture toughness of ceramic composites as function of microstructure: I. Numerical simulations." Journal of the Mechanics and Physics of Solids **61**(2): 472-488.

55. Li, Y. and M. Zhou (2013). "Prediction of fracturess toughness of ceramic composites as function of microstructure: II. analytical model." Journal of the Mechanics and Physics of Solids **61**(2): 489-503.

56. Liew, C., et al. (2001). "Dual material rapid prototyping techniques for the development of biomedical devices. Part 1: Space creation." The International Journal of Advanced Manufacturing Technology **18**(10): 717-723.

57. Liew, C. L., et al. (2002). "Dual material rapid prototyping techniques for the development of biomedical devices. Part 2: secondary powder deposition." The International Journal of Advanced Manufacturing Technology **19**(9): 679-687.

58. Liska, R., et al. (2007). "Photopolymers for rapid prototyping." Journal of Coatings Technology and Research **4**(4): 505-510.

59. Liu, A. F. (2005). Mechanics and mechanisms of fracture: an introduction, ASM International.

60. Ma, J., et al. (2004). "Effect of porous interlayers on crack deflection in ceramic laminates." Journal of the European Ceramic Society **24**(5): 825-831.

61. Mapili, G., et al. (2008). "Projection microfabrication of three-dimensional scaffolds for tissue engineering." Journal of Manufacturing Science and Engineering **130**: 021005-021001.

62. Masood, S. and W. Song (2004). "Development of new metal/polymer materials for rapid tooling using fused deposition modelling." Materials & design 25(7): 587-594.

63. McMeeking, R. and A. Evans (1982). "Mechanics of Transformation‐Toughening in Brittle Materials." Journal of the American Ceramic Society 65(5): 242-246.

64. Melchels, F. P., et al. (2010). "A review on stereolithography and its applications in biomedical engineering." Biomaterials 31(24): 6121-6130.

65. Meyers, M. A., et al. (2008). "Biological materials: structure and mechanical properties." Progress in Materials Science 53(1): 1-206.

66. Muju, S., et al. (1998). "Microcrack toughening in two-phase multilayered media." Acta materialia 46(15): 5385-5397.

67. Munch, E., et al. (2008). "Tough, bio-inspired hybrid materials." Science 322(5907): 1516-1520.

68. Murali, P., et al. (2011). "Role of modulus mismatch on crack propagation and toughness enhancement in bioinspired composites." Physical Review E 84(1): 015102.

69. Pandya, K. and J. Williams (2000). "Measurement of cohesive zone parameters in tough polyethylene." Polymer Engineering & Science 40(8): 1765-1776.

70. Peters, W. and W. Ranson (1982). "Digital imaging techniques in experimental stress analysis." Optical Engineering 21(3): 213427-213427-.

71. Pohanka, R. C., et al. (1978). "Effect of the phase transformation on the fracture behavior of BaTiO3." Journal of the American Ceramic Society 61(1-2): 72-75.

72. Qiao, P., et al. (2003). "Tapered beam on elastic foundation model for compliance rate change of TDCB specimen." Engineering Fracture Mechanics 70(2): 339-353.

73. Reddy, K. M., et al. (2012). "Enhanced mechanical properties of nanocrystalline boron carbide by nanoporosity and interface phases." Nature Communications 3: 1052.

74. Repetto, E., et al. (2000). "Finite element simulation of dynamic fracture and fragmentation of glass rods." Computer Methods in Applied Mechanics and Engineering 183(1): 3-14.

75. Sachs, E., et al. (1993). "Three-dimensional printing: the physics and implications of additive manufacturing." <u>CIRP Annals-Manufacturing Technology</u> **42**(1): 257-260.

76. Salmi, M., et al. (2013). "Accuracy of medical models made by additive manufacturing (rapid manufacturing)." <u>Journal of Cranio-Maxillofacial Surgery</u>.

77. Santosa, J., et al. (2002). "Experimental and numerical study on the flow of fine powders from small-scale hoppers applied to SLS multi-material deposition–part I." <u>Ann Arbor</u> **1001**: 48109-42125.

78. Segurado, J. and J. LLorca (2004). "A new three-dimensional interface finite element to simulate fracture in composites." <u>International journal of solids and structures</u> **41**(11): 2977-2993.

79. Shum, D. K. and J. W. Hutchinson (1990). "On toughening by microcracks." <u>Mechanics of Materials</u> **9**(2): 83-91.

80. Sih, G. C., et al. (1965). "On cracks in rectilinearly anisotropic bodies." <u>International Journal of Fracture Mechanics</u> **1**(3): 189-203.

81. Steinbrech, R. (1992). "Toughening mechanisms for ceramic materials." <u>Journal of the European Ceramic Society</u> **10**(3): 131-142.

82. Sutton, M., et al. (1983). "Determination of displacements using an improved digital correlation method." <u>Image and vision computing</u> **1**(3): 133-139.

83. Wicker, R., et al. (2004). <u>Multiple material micro-fabrication: extending stereolithography to tissue engineering and other novel application</u>. Proceedings of 15th Annual Solid Freeform Fabrication Symposium, Austin, TX, Wiley.

84. Wicker, R., et al. (2009). Multi-material stereolithography, Google Patents.

85. Wiederhorn, S. (1984). "Brittle fracture and toughening mechanisms in ceramics." <u>Annual Review of Materials Science</u> **14**(1): 373-403.

86. Wiria, F., et al. (2007). "Poly-< i> ε</i>-caprolactone/hydroxyapatite for tissue engineering scaffold fabrication via selective laser sintering." <u>Acta Biomaterialia</u> **3**(1): 1-12.

87. Wong, K. V. and A. Hernandez (2012). "A Review of Additive Manufacturing." <u>ISRN Mechanical Engineering</u> **2012**.

88. Xia, S., et al. (2007). "Delamination mechanism maps for a strong elastic coating on an elastic–plastic substrate subjected to contact loading." International journal of solids and structures **44**(11): 3685-3699.

89. Xia, S., et al. (2009). "Strength characterization of Al/Si interfaces: A hybrid method of nanoindentation and finite element analysis." Acta Materialia **57**(3): 695-707.

90. Yan, X. and P. Gu (1996). "A review of rapid prototyping technologies and systems." Computer-Aided Design **28**(4): 307-318.

91. Yang, B. and X. Chen (2000). "Alumina ceramics toughened by a piezoelectric secondary phase." Journal of the European Ceramic Society **20**(11): 1687-1690.

92. Yao, H., et al. (2013). "Cracks fail to intensify stress in nacreous composites." Composites Science and Technology.

93. Zhang, X., et al. (1999). "Micro-stereolithography of polymeric and ceramic microstructures." Sensors and Actuators A: Physical **77**(2): 149-156.

94. Zhang, Y., et al. (2001). "Rapid prototyping and combustion synthesis of TiC/Ni functionally gradient materials." Materials Science and Engineering: A **299**(1): 218-224.

95. Zhao, Y., et al. (2004). "Enhancement of fracture toughness in nanostructured diamond–SiC composites." Applied physics letters **84**(8): 1356-1358.

96. Zheng, G. and Y. Shen (2010). "Simulation of crack propagation in fiber-reinforced bulk metallic glasses." International Journal of Solids and Structures **47**(2): 320-329.